To the Graduate Council:

I am submitting herewith a thesis written by Tasha Laurrelle Dunn entitled "Identification of Terrestrial Alkalic Rocks Using Thermal Emission Spectroscopy: Applications to Martian Remote Sensing." I have examined the final paper copy of this thesis for form and content and recommend that it be accepted in partial fulfillment of the requirements for the degree of Master of Science, with a major in Geology.

Harry Y. McSween, Jr., Major Professor

We have read this thesis
and recommend its acceptance:

Jeffrey E. Moersch

Lawrence A. Taylor

Accepted for the Council:

Vice Chancellor and Dean of Graduate Studies

Thesis
2005
.D87

IDENTIFICATION OF TERRESTRIAL ALKALIC ROCKS USING THERMAL EMISSION SPECTROSCOPY: APPLICATIONS TO MARTIAN REMOTE SENSING

A Thesis
Presented for the
Master of Science
Degree
University of Tennessee, Knoxville

Tasha Laurrelle Dunn
December 2005

DEDICATION

This thesis is dedicated to my parents, Roy and Sherry Dunn, for their unrelenting love and support, and to my sister, Andrea, who shows me everyday what it means to be strong.

In loving memory of John A. Johnson and Roy S. Dunn, Sr.

ACKNOWLEDGMENTS

I would like to thank my advisor, Dr. Harry "Hap" McSween, for bringing me to the University of Tennessee in the first place, and for his guidance in the development and completion of this project. Thanks also to Hap for his willingness to serve as my advisor in the coming years. I would also like to acknowledge my committee members, Dr. Larry Taylor, for helping me to become a more confident scientist, and Dr. Jeff Moersch, for introducing me to the many applications of remote sensing.

There are several people that have assisted me in various aspects of this project to whom I owe a great deal of gratitude. Special thanks to Allan Patchen for his supervision and assistance in using the electron microprobe. Thanks also to Keith Milam, an exceptional scientist who graciously taught me the fine art of collecting, processing, and deconvolving thermal emission spectra. Thanks also to Bill Deane for his help in gathering XRF and XRD data and for the support he provides to all members of the planetary research group. I also would like to acknowledge Dr. Hanna Nekvasil of the State University of New York for graciously loaning us the Nandewar volcano samples and Dr. Jeffrey Post, curator of the mineral collection at the Smithsonian Institute, for providing requested mineral samples.

Finally, thanks to my fellow graduate students for their support and friendship. Thanks especially to Rhiannon Mayne, Dr. Karen Stockstill, and the rest of the girls for many memorable evenings together.

ABSTRACT

We present a detailed study examining the use of laboratory thermal emission spectra (5-25 μm at 2 cm^{-1} spectral sampling) for identification and classification of alkalic volcanic rocks. Modal mineralogies and derived bulk rock chemistries of a suite of terrestrial alkali basalts, trachyandesites, trachytes, and rhyolites were determined using linear spectral deconvolution. Model-derived mineral modes were compared to modes measured using an electron microprobe mapping technique to access the accuracy of linear deconvolution in determining mineral abundances. Standard deviations of 1σ of absolute differences between measured and modeled mineral abundances range from 0.68 to 15.02 vol %, with an average of 5.67 vol %. Bulk-rock chemistries were derived by combining modeled end-member compositions (wt %) in proportion to their abundances (recalculated to wt %). Derived oxide data compare well with measured oxide data, with 1σ standard deviations ranging from 0.12 to 2.48 wt %. Modeled mineralogies, derived mineral chemistries, and derived bulk chemistries were examined to assess their accuracy in classifying alkalic rocks. Derived bulk chemistry is the most effective classification tool, modal mineralogy is the least, and basalts and rhyolites are typically more accurately classified than trachyandesites and trachytes. However, no single classification scheme can accurately identify all rock samples, indicating that a combination of classification schemes is necessary to distinguish alkalic volcanic rocks using thermal emission spectra. To examine the accuracy of volcanic rock classification at lower spectral resolutions, thermal emission spectra were resampled to the resolution of the Thermal Emission Spectrometer (TES) instrument (10 cm^{-1}), and a second series of linear deconvolutions was performed. Results from modeled mineralogies and derived

bulk-rock chemistries at 10 cm^{-1} are comparable to results at 2 cm^{-1} spectral sampling, indicating that this amount of degradation of spectral sampling does not adversely affect modal mineralogies and chemistries derived from linear deconvolution. Data from 10 cm^{-1} spectral sampling were applied to derived mineral and bulk chemistry classification schemes with high degrees of success. Overall, results from this study suggest that linear deconvolution of thermal emissivity spectra can be successfully applied to the identification and classification of alkalic volcanic rocks on Mars.

TABLE OF CONTENTS

Chapter Page

1. Introduction 1

1.1. Thermal Infrared Spectroscopy 1

1.2. Applications of TIR Spectroscopy to Martian Remote Sensing 2

1.3. Classification of Volcanic Rocks Using TIR Spectroscopy 6

2. Rock Samples 9

2.1. Basalts 10

2.2. Trachyandesites 10

2.3. Trachytes 11

2.4. Rhyolites 11

3. Experimental and Analytical Techniques 12

3.1. Modal Mineralogy 12

3.2. Geochemistry 13

3.3. Spectral Analysis 13

3.4. Linear Deconvolution 15

3.4.1. Description 15

3.4.2. End-member selection 16

3.4.3. Application 17

4. Results 19

4.1. Measured and Modeled Spectra 19

4.2. Mineralogy 20

4.3. Derived Chemistry 24

4.3.1. Alkali feldspar compositions 25

4.3.2. Plagioclase feldspar compositions 27

4.3.3. Pyroxene compositions 28

4.3.4. Derived bulk rock chemistry 30

5. Volcanic Rock Classification 33
5.1. Deconvolved Modal Mineralogy 33
5.2. Derived Mineral Chemistry 33
5.3. Derived Bulk Rock Chemistry 34
5.4. Summary of Classifications 36
6. Applications to Martian Remote Sensing 37
6.1. Deconvolution of Rock Compositions at TES Resolution 37
7. Conclusions 46
References 48
Appendix 55
Tables 56
Figures 70
Vita 93

LIST OF TABLES

Table		Page
1.	Major and Minor Element Analyses of Nandewar Alkalic Rocks	56
2.	Classification of Nandewar Alkalic Rock Samples	57
3.	Concentration Criteria Used to Classify Minerals and Glasses	58
4.	Major Element Analysis of Minerals Added to the Spectral Library	59
5.	End-member Mineral Compositions Used in Deconvolutions	60
6.	Electron Microprobe Measured Mineralogy	62
7.	Deconvolved Bulk Mineralogy at 2 cm^{-1} Spectral Sampling	63
8.	Major Mineralogy and Bulk-Rock Chemistry Error Analysis	64
9.	Compositions of Glass Spectral End-members and Nandewar Glass	65
10.	Summary of Volcanic Rock Classifications	66
11.	Deconvolved Bulk Mineralogy at 10 cm^{-1} Spectral Sampling	67
12.	Comparison of Uncertainties at 2 cm^{-1} and 10 cm^{-1} Spectral Sampling	68
13.	Modal Mineralogies Derived From Martian Surface Spectra	69

LIST OF FIGURES

Figure Page

1. Thermal emissivity spectra of common rock-forming silicate minerals [*Christensen et al.*, 2000]……70
2. Four major trends of alkalic hot spot volcanism [from *Nekvasil et al.*, 2003]…..71
3. Fractional crystallization sequence of Gusev Crater basalt *Humphrey* modeled using MELTS program, developed by *Ghiorso and Sack* [1995]……72
4. Chemical compositions of Nandewar volcano alkalic rocks examined in this study……..73
5. Measured (black) and modeled (purple) thermal emissivity spectra of (a) basalts, trachyandesites, mafic trachytes, and (b) peralkaline trachytes and rhyolites 74
6. Comparison of electron microprobe (measured) and deconvolved bulk mineralogies for (a) basalts, trachyandesites, mafic trachytes, and (b) peralkaline trachytes and rhyolites……...76
7. Or-Ab-An ternary diagram showing measured (enclosed areas) and model-derived (symbols) alkali and plagioclase feldspar compositions for basalts, trachyandesites, trachytes, and rhyolites. ……..78
8. Deconvolved (closed symbols) and measured (open symbols) pyroxene compositions for (a) basalts and trachyandesites and (b) trachytes and rhyolites in the diopside (Di)- enstatite (En)- hedenbergite (Hd)- ferrosilite (Fs) system……79
9. Measured versus derived oxide data (wt %) for basalts, trachyandesites, trachytes, and rhyolites……..80

10. Model-derived modal mineralogies of basalts, trachyandesites, trachytes, and rhyolites samples.....81

11. Normative plagioclase compositions (mol % An) versus normative color index (modal olivine + pyroxene + amphibole) for separating alkaline volcanic rocks [*Irvine and Baragar,* 1971].....82

12. Measured (closed symbols) and modeled (open symbols) chemical compositions of basalts, trachyandesites, trachytes, and rhyolites.....83

13. Derived (open symbols) and measured (closed symbols) silica and alkali oxides superimposed on the *Cox et al.* [1980] classification scheme for volcanic rocks 84

14. Measured (black) and modeled (purple) thermal emissivity spectra at 10 cm^{-1} resolution of (a) basalts, trachyandesites, mafic trachytes, and (b) peralkaline trachytes and rhyolites.....85

15. Comparison of modal mineral abundances (vol %) at 2 cm^{-1} and 10 cm^{-1} spectral sampling.....87

16. Measured versus derived oxide data (wt %) for basalts, trachyandesites, trachytes, and rhyolites at 2 cm^{-1} and 10 cm^{-1} spectral sampling.....88

17. Normative plagioclase compositions (mol % An) versus normative color index (modal olivine + pyroxene + amphibole) [*Irvine and Baragar,* 1971] for data at 10 cm^{-1} spectral sampling.....89

18. Derived chemical compositions of alkalic rocks at 2 cm^{-1} (open symbols) and 10 cm^{-1} (closed symbols) spectral sampling.....90

19. TES martian surface spectra (black) [*Bandfield et al.*, 2000a] and modeled spectra (purple) derived using our alkalic rock end-member set.....91

20. Chemical classification of martian surface type 1 and 2 spectra derived using alkalic end-members.....92

1. INTRODUCTION

1.1. Thermal Infrared Spectroscopy

Many remote sensing instruments detect wavelengths of the electromagnetic spectrum that are outside of the range visible to the human eye. In this range, many materials have unique spectra that reflect their compositional and structural variations; thus, non-visible wavelengths can be used to identify various materials. Minerals can be identified using various wavelengths ranging from Shortwave Infrared (SWIR) (1-3 μm) to Thermal Infrared (TIR) (~5-50 μm). However, certain wavelengths are better suited for the detection of various types of minerals than are others. For example, clay minerals are best detected at SWIR wavelengths, while silicate minerals are more easily recognized in the TIR wavelengths.

Many common rock-forming minerals have absorption features in the TIR range (Figure 1). (See Appendix for all figures and tables.) Silicate minerals have characteristic absorption features associated with stretching of Si-O bonds between 8-12 μm, whereas absorbance features in carbonates, which are found between 6-8 μm, result from vibrational transitions related to C-O bonds. Clays also have absorption features in the TIR associated with stretching of the O-OH bond. Because a variety of minerals have absorption features in the TIR, an unknown mineral spectrum can be easily identified by accurate recognition of prominent absorption features. Thermal infrared wavelengths are commonly used in extraterrestrial remote sensing of planetary surfaces because silicate minerals dominate the majority of igneous rock compositions.

In a complex mixture, such as a rock, spectral features of individual minerals or phases add linearly to produce a mixed spectrum [*Thomson and Salisbury,* 1993].

Therefore, a complex mixture can be identified by breaking down the unknown spectrum into its individual mineral components using linear deconvolution, a technique based on the principle that the energy emitted from a mixed TIR spectra is equivalent to the energy of its components in proportion to their areal percentage [e.g. *Thomson and Salisbury,* 1993*; Ramsey and Christensen,* 1998]. Deconvolved mineral spectra are identified using a library of known spectral end-members [*Johnson et al.,* 1983, 1992*; Hamilton et al.,* 1997*, Ramsey and Christensen,* 1998*, Feely and Christensen,* 1999*; Christensen et al.,* 2000; *Hamilton and Christensen,* 2000]. Model-derived modal mineralogy and bulk-rock chemistry derived by combining modeled end-member compositions (wt %) in proportion to their abundance in a rock (recalculated to wt %) are then used to identify the unknown mixed spectrum.

1.2. Applications of TIR Spectroscopy to Martian Remote Sensing

The Mars Global Surveyor (MGS) spacecraft was launched by NASA in November 1996 and arrived in Martian orbit in September 1997. The Thermal Emission Spectrometer (TES) is one of several scientific instruments onboard MGS. TES uses thermal infrared energy emitted from the Martian surface to identify rock compositions and surface lithologies [*Bandfield et al.,* 2000a*; Hamilton and Christensen,* 2000*; Christensen et al.,* 2001]. TES is a Fourier transform Michelson interferometer that collects spectra over a wavelength range of 5.8-50 μm (1709-200 cm^{-1}) at a spectral sampling of 5 and 10 cm^{-1} and a spatial resolution of 3x5 km. The TES instrument is calibrated by collecting reference spectra from both an internal reference surface and outer space. These spectra, which are collected as radiance values, are then converted to emissivity (ϵ), which is preferred over radiance because it is not affected by changes in

temperature. The conversion to emissivity is accomplished by dividing radiance by the Planck function at the radiative temperature of the surface, which is determined using methods described by *Christensen et al.* [2001]. After temperature effects are removed, atmospheric dust, CO_2, and H_2O contributions are also removed, leaving only desired geologic compositional information in the emissivity spectra. Methods for removing atmospheric contributions are described by *Bandfield et al.* [2000b] and *Smith et al.* [2000].

TES analyses have identified two widespread, compositionally distinct surface types on Mars [*Christensen et al.*, 2000a; *Bandfield et al.*, 2000a; *Christensen et al.*, 2001; *Wyatt and McSween,* 2002]. Christensen et al. [2000a] identified a basaltic component in Cimmeria Terra, whereas *Bandfield et al.* [2000a] recognized two distinct global surface lithologies. Surface type 1 has been identified as basalt, and surface type 2 has been suggested to be either andesite [*Bandfield at al.,* 2000a] or partially weathered basalt [*Wyatt and McSween,* 2002]. Both surface types are roughly separated by the Martian crustal dichotomy. Surface type 1 is found in the older, heavily cratered southern highlands, and surface type 2 is located in the younger plains of the northern lowlands [*Bandfield et al.,* 2000a]. Both surface types are dominated by plagioclase and clinopyroxene [*Bandfield et al.,* 2000a]. Deposits of hematite [*Christensen et al.,* 2000b] and some olivine [*Hoefen et al.,* 2003; *Hamilton and Christensen*, 2005] have also been identified.

Although volcanic surface compositions identified using TES are subalkaline, several lines of evidence from martian SNC meteorites and from rocks examined by the Mars Exploration Rover (MER) suggest alkalic magmatism may have once been active

on Mars. Non-feldspathic glass in Chassigny polyphase melt-inclusions is an alkali-enriched rhyolite glass, similar to that found in rhyolites of sodic silica-saturated alkalic magmatic suites [*Johnson et al.,* 1991; *Nekvasil,* 2003]. Mineral assemblages and LREE enrichment signatures of the Chassigny meteorite are comparable to those of intra-plate terrestrial magmas [*Nekvasil et al.,* 2003], suggesting that Chassigny may have formed from magmatic processes indicative of sodic silica-saturated alkalic volcanism (Trend 1 in Figure 2) [*Nekvasil et al.,* 2003].

Evidence for alkalic volcanism has also been found in martian basalts examined by the MER Spirit at the Gusev Crater landing site. Crystallization modeling using MELTS, developed by *Ghiorso and Sack*, 1995, indicates that low pressure (1 atm) fractional crystallization of the martian rock Humphrey produces a liquid line of descent with an alkalic trajectory (Figure 3). Using the composition of Humphrey, the modeled liquid path travels through the basalt field and into the trachybasalt and basaltic trachyandesite fields before terminating in the trachyandesite field. This suggests that fractional crystallization of some martian basalts may yield alkalic compositions. These data, along with geochemical evidence from Chassigny, indicate that martian volcanism may not have been strictly subalkaline, as current remote sensing data would suggest.

The division between alkalic and subalkaline rocks reflects different chemical and mineralogical attributes in igneous rocks found in distinct geologic settings. Chemically, the basic difference between the two rock groups is their concentrations of silica relative to alkalis. Alkalic rocks are deficient in silica relative to other elements, whereas subalkaline rocks are saturated in SiO_2. Chemically, subalkaline rocks cannot evolve to alkalic rocks; the reverse is also true. Whether subalkaline or alkalic magmas are

produced is a result of conditions in the mantle, such as pressure, temperature, and degree of partial melting. Alkalic rocks are produced at greater depths than subalkaline rocks, reflecting partial melting at increased pressure. At constant pressure, subalkaline rocks form as a result of higher degrees of partial melting. Alkalic rocks also form when the mantle source region has undergone metasomatism (alteration by interaction with fluids), which commonly increase alkalis.

Volumetrically, subalkaline rocks are the most common igneous rocks on Earth. They are found in most geologic environments, with the tholeiitic members located primarily in mid-ocean ridge spreading centers and convergent plate boundaries, and the calc-alkaline members located predominantly in orogenic belts and at convergent plate boundaries. Alkalic rocks are found almost exclusively in intra-plate continental and oceanic regions, and only rarely occur at plate boundaries. Compositions vary as a function of location, as those found in oceanic regions are sodic, while those located in continental regions are potassic or sodic.

The composition of a rock, whether subalkalic or alkalic, provides substantial information regarding its petrogenesis, including the type of geologic and tectonic environment in which the magma formed. This information is particularly important when dealing with a sample from a planet such as Mars, where past geologic or tectonic conditions are not well understood. The potential identification of alkalic rocks on Mars would significantly alter our current understanding of martian geologic history, providing new insight into martian volcanism and magmatic processes.

1.3. Classification of Volcanic Rocks Using TIR Spectroscopy

Before TES can be used effectively to search for alkalic rocks, it must first be determined if linear deconvolution of thermal emissivity spectra can successfully distinguish between subalkalic and alkalic rocks, and if model-derived modal mineralogy and bulk rock chemistry can be used to accurately classify alkalic rocks based on terrestrial classification schemes. One of the most commonly used classification schemes is the IUGS system [*Streckeisen*, 1976; *LeMaitre*, 1989], which distinguishes plutonic and volcanic igneous rocks based on the modal abundances of quartz, plagioclase, and alkali feldspar or feldspathoids present. Because modal mineralogy is traditionally determined using optical point-counting methods, fine-grained groundmass material often remains unquantified. This results in unrepresentative bulk-rock mineralogies that may be misleading for classification purposes. Volcanic rocks are typically fine-grained and often contain large amounts of mesostasis or glass, and are, therefore, difficult to classify accurately based on modal mineralogy. As a result, volcanic igneous rocks are usually classified based on chemistry rather than mineralogy [e.g., Cox et al., 1980]. The most common classification scheme for volcanic rocks used today was developed by *Le Bas et al.* [1986]. Using this classification scheme, alkalic rocks are distinguished from subalkaline rocks on the basis of alkali ($Na_2O + K_2O$) and silica (SiO_2) abundances. Alkalic rocks are undersaturated in SiO_2 relative to their other components, especially Na_2O and K_2O.

It is difficult to apply terrestrial chemical classification schemes to extraterrestrial rocks because of a lack of complete mineralogical data available from remote sensing techniques. Previous studies have attempted to develop classification schemes for

extraterrestrial igneous rocks, with varying degrees of success. *Walter and Salisbury* [1989] developed a generalized classification scheme for distinguishing igneous rocks using mid-infrared spectra, in which rocks were identified using statistical analysis of average band intensities versus SCFM, a chemical parameter that describes the average polymerization of a sample based on its primary cation (Ca, Fe, or Mg) content relative to silica. The *Walter and Salisbury* study examined a wide compositional range of volcanic and plutonic igneous rocks, but failed to address the issue of discriminating between samples with similar compositions and was also only applicable to unweathered samples.

Wyatt et al. [2001] examined the accuracy of using thermal infrared emission spectra to identify and classify a smaller compositional range of subalkaline volcanic rocks, ranging from basalt to dacite. Modal mineralogies were determined directly from linear spectral deconvolution, and bulk-rock chemistries were calculated from modeled mineralogies. Modeled mineralogies and chemistries were used to access the accuracy of subalkaline volcanic rock classifications. Results from *Wyatt et al.* [2001] and a companion study by *Hamilton et al.* [2001] indicate that linear deconvolution of thermal emissivity spectra can successfully be applied to classification of subalkaline volcanic rocks at both laboratory resolution (2 cm^{-1}) and TES instrument resolution (10 cm^{-1}). These studies did not attempt, however, to classify alkalic volcanic rocks. Before a complete assessment of using the linear deconvolution method to classify volcanic rocks can be made, the full compositional range of volcanic igneous rocks must be examined.

This study follows closely on *Wyatt et al.* [2001], employing the same methods to determine if infrared spectra of terrestrial alkali basalts, trachyandesites, trachytes, and rhyolites can be used for petrologic classification. We also address whether degradation

of thermal emission spectra from laboratory resolution (2 cm^{-1}) to TES instrument resolution (10 cm^{-1}) adversely affects model-derived mineralogies, chemistries and volcanic rock classifications. Finally, we apply our results to current martian remote sensing applications by deconvolving TES surface type 1 and 2 spectra [*Bandfield et al.*, 2000a] using a set of end-members tailored for alkalic rock compositions.

2. ROCK SAMPLES

A suite of 11 volcanic rocks from the Nandewar volcano in north-eastern New South Wales, Australia was provided by Hanna Nekvasil of SUNY Stony Brook. The Nandewar volcano was a region of widespread alkalic volcanism during the Tertiary, producing lavas with compositions ranging from olivine basalt to alkali rhyolite. Selected samples, which are relatively unweathered and unaltered, include two basalts (a hawaiite and a trachybasalt), two trachyandesites, four trachytes, and three rhyolites [*Abbott,* 1969*; Stolz,* 1985, 1986]. Together these rocks represent the complete fractional crystallization sequence of sodic, silica-saturated alkalic rocks. This type of silica-saturated alkalic volcanism is common at continental hot-spots such as the Nandewar volcano, and represents trend 1 of the four major trends of alkalic volcanism (Figure 2). Major element analyses for rocks in this study, as well as sources of data, are presented in Table 1.

Abbott [1969] and *Stolz* [1985, 1986] employed several different criteria for classifying the Nandewar rock samples [e.g. *Coombs and Wilkinson*, 1969; *Macdonald and Katsura*, 1964; *MacDonald and Bailey,* 1973]. Since that time, modern classification schemes for classifying volcanic rocks have been developed and are routinely used [e.g., *Le Bas et al.,* 1986]. For this study, samples were reclassified using the Le Bas chemical classification system based on the abundance of silica and alkali oxides (Figure 4). Original sample classifications do not change for trachytes and rhyolites; however, minor changes do occur in samples originally classified as hawaiites, trachyandesites, and tristanites. Table 2 lists both original and chemical sample classifications.

2.1. Basalts

Sample 49000 was originally classified as hawaiite [*Abbott,* 1969], a term used to describe a differentiated basaltic lava containing modal or normative andesine. Chemical classification [*Le Bas et al.,* 1986] indicates sample 49000 is a basalt. Sample 49000 is porphyritic and contains phenocrysts of olivine (Fa_{23}) and plagioclase (An_{60}) in a groundmass of clinopyroxenes, plagioclase laths, and titanomagnetite [*Abbott,* 1969; *Stolz,* 1985, 1986]. Sample 49005, originally termed a trachyandesite [*Abbott,* 1969], is chemically classified as a trachybasalt. This sample consists primarily of the same minerals as basalt 49000 (plagioclase, olivine, clinopyroxene, and some alkali feldspar), but does not contain large phenocrysts of olivine and plagioclase. Although both samples have similar mineralogies, their chemical classifications differ as a result of alkali oxide abundances. Both samples will be referred to as basalts throughout this study.

2.2. Trachyandesites

Compositionally, trachyandesites have mineralogies similar to those of basalts. The Nandewar trachyandesites are dominated by phenocrysts of plagioclase, olivine, amphiboles, and clinopyroxene in a fine-grained groundmass of plagioclase laths, augite, Fe-oxides, and apatite [*Abbott,* 1969; *Stolz,* 1985, 1986]. Sample 49012, classified as a trachyandesite by *Abbott* [1969], is classified as a basaltic trachyandesite using the chemical classification scheme [*Le Bas et al.,* 1986]. Sample 49074, originally classified using the term tristanite, is chemically described as a trachyandesite. Both samples will be referred to as trachyandesites throughout this study.

2.3. Trachytes

Two types of trachytes are present within the Nandewar crystallization series, mafic trachytes (samples 49083 and 15800) and peralkaline trachytes (samples 49098 and 15802). All trachytes consists primarily of feldspar (>80%), with the remainder comprised of pyroxenes and amphiboles. The Nandewar mafic trachytes consists of two or more feldspars, usually oligoclase and anorthoclase, which occur both as phenocrysts and as groundmass material. The remainder of the groundmass is comprised of augite, alkali amphibole, titanomagnetite, and ilmenite [*Abbott,* 1969*; Stolz,* 1985, 1986]. The peralkaline trachytes are more differentiated than their mafic counterparts, consisting of only one feldspar, either sanidine or anorthoclase. Aegerine-augite and ferrohedenbergite are the dominant pyroxenes, and amphiboles with compositions ranging from riebeckite to arfvedsonite are sometimes present. Aenigmatite and minor amounts of titanomagnetite and quartz comprise the remaining groundmass material [*Abbott,* 1969*; Stolz* 1985, 1986]. Texturally, the trachytes are most often porphyritic or aphanitic.

2.4. Rhyolites

The extreme differentiates in the Nandewar series are rhyolites (samples 15806, 15807, and 49130). The rhyolites are composed predominantly of one feldspar, either sanidine or anorthoclase, and quartz [*Abbott,* 1969]. Samples 15806 and 15807 are peraluminous rhyolites, which are characterized by the presence of mafic minerals such as aegerine-augite, alkali amphiboles, and aenigmatite [*Abbott*, 1969; *Stolz*, 1985; 1986]. Sample 49130 is a porphyritic peralkaline rhyolite. Alkali rhyolites are composed entirely of alkali feldspar and quartz; mafic minerals are not present in this type of rhyolite.

3. Experimental and Analytical Techniques

3.1. Modal Mineralogy

The accuracy of deconvolved mineralogies is determined by comparing modeled modes to modes obtained using an electron microprobe phase-mapping technique. Modes determined using microprobe mapping are comparable to those derived from spectral deconvolution because both techniques report areal abundances (stated as vol %). Mineral phases that may be too small to identify using traditional point-counting methods can be accurately measured using this phase-mapping technique.

Mineral abundances were measured using an Oxford Instruments (LINK) Model eXL II energy dispersive spectrometer (EDS) mounted on a Cameca SX-50 electron microprobe at the University of Tennessee. Prior to phase mapping, polished thin sections were studied using transmitted and reflected light to identify all minerals present. Modal mineralogies were determined using a microanalysis technique [*Taylor et al.*, 1996], in which the Feature Scan image analysis software package is used to detect, measure, and analyze phases present in a backscattered electron (BSE) image. Mineral phases appear as distinct shades of grey in a BSE image (the result of variations in average atomic number), allowing for ready identification of minerals. Various phases were distinguished by defining "windows" of the energy dispersive spectrum (e.g., 1.38-1.60 keV for Al). A combination of "windows" was used as identification criteria for a mineral phase (Table 3). For example, criteria indicative of alkali feldspar include high Al, high K, and low Ca. Identification criteria were established after several analyses of each phase were taken to determine approximate chemical composition.

EDS X-ray data were collected using a 4 nA beam current, a 1 μm beam size, an excitation potential of 20 eV, and a counting time of 40-60 x 10^{-3} s. An EDS spectrum was collected along a grid of 60-70 fields per sample, resulting in the classification of more than 200,000 pixels per thin section, significantly more than traditional optical point-counting. Pixels that were unclassified (on average < 10%) typically fell on grain boundaries or along fractures, and modes were recalculated to 100% based on the assumption that unclassified pixels were random. The microanalysis technique has an estimated precision of at least 5 % of the amount of each phase present [*Taylor et al.*, 1996].

3.2. Geochemistry

Bulk-rock and mineral chemistry of rock samples were determined in previous studies [*Stolz,* 1985, 1986*; Abbott,* 1969]. Chemistries of minerals added to the spectral library in this study were determined using X-ray fluorescence (XRF) (Table 4) at the University of Tennessee. To achieve the most accurate analysis, a fused glass bead of each mineral sample was prepared by combining 1 g of powdered mineral sample with 0.0130 g of lithium iodide, 0.0500 g of ammonium nitrate, and 5.500 g of lithium tetraborate. The mixture was then agitated to insure homogeneity and melted at 1100°C using a Philips Perl' x 3. The liquid mixture was then allowed to cool and solidify. Analyses were completed using a Phillips Analytic MagixPro following procedures outlined in *Norrish and Hutton* [1969].

3.3. Spectral Analysis

Thermal emission spectra of rock and mineral samples were collected using a Nicolet Nexus 670 spectrometer at Arizona State University, following a technique

described by *Ruff et al.* [1997]. In preparation for thermal emission spectroscopy, mineral samples were ground into particulate material using a mortal and pestle. Material was then sieved, and grains ranging in size from 500 to 1000 μm were separated for use. Grains of this size are traditionally used for thermal infrared spectroscopy because coarse sand is the dominant grain size of Martian surface material examined in the thermal infrared. Coarse sand particles are also preferred because they are oriented randomly during spectral measurements, eliminating potential grain orientation effects [*Ruff,* 1998], and because their particle diameter is larger than wavelength of the emitted thermal infrared photons, which is necessary to avoid reduced spectral contrast and spectral features unique to fine-grained samples [*e.g. Salisbury and Wald,* 1992*; Moersch and Christensen,* 1995*; Hamilton,* 1999]. Particles with visible impurities were removed from the particulate mineral samples, and samples were washed once with tap water and then twice with deionized water. Samples were then dried at 77°C for 72 hours and placed in 3 cm diameter sample cups. Rock samples required no advance preparation, as spectra were obtained from a fresh surface (3-4 cm in diameter). Immediately prior to analysis, both rock and mineral samples were heated to 80°C for 12 hours to enhance the signal to noise ratio in the spectrum.

Spectral data were collected over a wavelength range of 2000-200 cm^{-1} (2.5- 50 μm) at a sampling of 2 cm^{-1}. The TES instrument covers a smaller wavelength range (1650-200 cm^{-1}) at a reduced spectral sampling of 10 cm^{-1}. Because of the difference between laboratory and TES wavelengths, data collected over wavelengths of 1650 to 2000 cm^{-1} are not pertinent to this study and were discarded. Raw radiance data were then converted to emission spectra using techniques developed by *Christensen and*

Harrison [1993] and modified by *Ruff et al.* [1997]. Sources of instrument-derived error in data acquisition for any given spectrum are ~2-5 % absolute emissivity [*Ruff et al.,* 1997].

3.4. Linear Deconvolution

3.4.1. Description

An algorithm for linear deconvolution of thermal infrared emission spectra was presented by *Ramsey and Christensen* [1998]. This algorithm, which is used in this study, requires three inputs: a spectrum to be deconvolved, a library of pure mineral spectra (end-members), and a wavelength range over which to perform the fit. In this study, mineral spectra from the Arizona State University (ASU) spectral library [*Christensen et al.,* 2000] were used as end-members and fitting was constrained to 400-1300 cm^{-1} to avoid water vapor and CO_2 features. Outputs from the algorithm include the percentage of each end-member, a best-fit modeled spectrum, and a root-mean-square (RMS) error value, which is the average error over the entire spectral region. The RMS value is used as an indicator of goodness of fit, or how well a modeled spectrum reproduces the original rock spectrum being deconvolved. RMS errors, however, cannot be used to compare goodness of fit between different samples [*Ramsey and Christensen,* 1998; *Hamilton and Christensen,* 2000]. Application of the linear deconvolution technique to thermal emission spectra of coarse-grained particulate samples is described by *Ramsey and Christensen* [1998], and application to solid rock samples by *Hamilton et al.,* [1997], *Feely and Christensen* [1999], *and Hamilton and Christensen* [2000].

3.4.2. End-member selection

Accurate linear deconvolution of a mixed spectrum is largely dependent on the selection of mineral end-members used as inputs during the deconvolution. In order to produce an accurately modeled spectra, the approximate range of compositions present in the sample must be present as end-members [*Hamilton et al.,* 1997*; Feely and Christensen,* 1999]. It is unlikely that every phase present in an unknown rock will be modeled accurately with a single end-member, even when a comprehensive selection of appropriate end-members is available. This is most common in solid-solutions, such as plagioclase, pyroxene, and olivine. However, a single compositionally equivalent end-member can be reproduced if several compositionally related end-members are summed in proportion to reproduce the unknown phase. *Hamilton et al.* [1997], *Hamilton and Christensen* [2000], and *Milam et al.* [2004] have demonstrated that the compositions of olivine, pyroxene, and plagioclase can be modeled with some accuracy by combining the spectra of two or more solid-solution minerals to produce an intermediate composition. The end-members used in this study are from the ASU spectral library [*Christensen et al.,* 2000]. A blackbody end-member is also used to account for variations in spectral contrast [*Hamilton et al.,* 1997*; Freely and Christensen,* 1999*; Hamilton and Christensen,* 2000].

The abundance of a phase cannot be modeled accurately if there is a complete absence of a compositionally or structurally similar phase in the mineral library. In this case, some or all of the modeled phases will have inflated abundances due to redistribution of unmodeled phases into the derived modes, which the algorithm calculates as percentages that sum up to 100 vol % [*Ramsey and Christensen,* 1998]. In

this study, several alkalic amphiboles and pyroxenes, for which spectra were previously underrepresented, were added to the mineral library. These minerals were observed in the Nandewar rock samples during initial analyses [*Abbott,* 1969*; Stolz,* 1985, 1986] and the presence of compositionally similar phases was confirmed by electron microprobe phase mapping. As part of this study, three pyroxenes and two amphiboles were added to the ASU mineral library. Pyroxenes and amphiboles added to the mineral library include omphacite, aegirine, aenigmatite, richterite, and arfvedsonite, all of which are phases rich in sodium and calcium, and common to alkalic rocks. Sanidine feldspar was also added to the spectral library. Prior to this study, sanidine was the only feldspar not available in the ASU spectral library. Sanidine is the predominant feldspar in the Nandewar volcano trachytes and rhyolites, and although sanidine compositions may be reproduced by combining end-members already present in the mineral library, the addition of this phase completes the feldspar solid solution series and should result in more accurately modeled feldspar compositions. Mineral samples were provided by the Smithsonian Institution in Washington, D.C. Bulk chemistries for minerals added to the spectral library are presented in Table 4.

3.4.3. Application

To provide the best constraints on bulk mineralogy, the linear deconvolution algorithm was run twice for each sample. Initially, each sample spectrum was deconvolved at laboratory resolution (2 cm^{-1}) using the entire ASU spectral library (over 200 endmembers) [*Christensen at al.,* 2000] and the mineral endmembers added in this study. As a result of using an expansive spectral library, minerals are often modeled in small abundances that are not likely present in a rock to improve the spectral fit.

Therefore, models using the full spectral library are difficult to interpret. To reduce this effect, a second deconvolution was performed using a set of endmembers representing the most abundant phases modeled in the initial deconvolution. These phases consist of common rock-forming minerals, including alkali feldspar, plagioclase, quartz, pyroxenes, and amphiboles, and minerals found predominantly in alkalic rocks, such as Ca-Na amphiboles and pyroxenes. Oxide minerals, such as hematite and ilmenite, were not included in this deconvolution because they are spectrally flat over most of the wavelength region of interest. This behavior can result in the modeling of an oxide component rather than a blackbody. Compositions of end-members used in linear deconvolutions are listed in Table 5.

4. RESULTS

Linear deconvolution-derived modal mineralogies of basalts, trachyandesites, trachytes, and rhyolites were compared to laboratory-measured modes. Mineral and bulk-rock chemistries derived from modal mineralogy were also compared to laboratory-measured bulk rock and mineral chemistries [*Abbott,* 1969*; Stolz,* 1985, 1986] to assess the accuracy of the linear deconvolution method in determining mineralogy and chemistry. Bulk-rock chemistries of all samples are shown in Table 2, and electron microprobe-measured modal mineralogies are displayed in Table 6.

Measured mineralogy indicates that alkali feldspar is the most abundant phase measured in trachyandesites, trachytes, and rhyolites, while plagioclase is the dominant phase in basalts. Variable amounts of silica-K_2O glass (6-58 vol %) are present in most samples, whereas silica-rich glass is present only in peralkaline trachytes and rhyolites. Small amounts of quartz (3-4 vol %) are present in peralkaline trachytes with increasing abundances present in rhyolites (2-24 vol %). Clinopyroxene is present in basalts, trachyandesites, and mafic trachytes at abundances ranging from 2-16 vol %. Amphibole is present in all rock groups, but is most common in peralkaline trachytes and rhyolites, where abundances average 2 vol %. 9 to 12 vol % olivine is present in both basalt samples, while a small abundance (2 vol %) is found in one trachyandesite sample. In samples where olivine occurs, low abundances of apatite are also present. Fe-oxides are present in all groups except for rhyolites at abundances averaging ~3.5 vol %.

4.1. Measured and Modeled Spectra

Measured and modeled spectra of basalt, trachyandesites, trachytes, and rhyolites are shown in Figure 5. Differences in positions and relative depths of absorbance

features between rock types are the result of variations in abundances and compositions of mineral phases. Likewise, dissimilarities between mineralogies within a rock group also produce slight spectral variations. Overall, spectral fits produced by the linear deconvolution algorithm are good. RMS errors range from 0.307 to 0.519, with the exception of one trachyte sample with an RMS error of 0.613. This suggests that major rock minerals are well represented in the spectral library and provide good fits for rocks in this study. Misfits do occur, primarily in the regions between 1200-800 cm^{-1} and 600-400 cm^{-1}. The most prominent misfit is the presence of an unmeasured absorbance feature at ~875 cm^{-1} in several samples (Figure 5). The causes of these misfits are discussed in section 5.2, as modeled phases abundances are compared to measured values to assess their accuracy.

4.2. Mineralogy

Model-derived bulk mineralogies (total 100%) for all samples are presented in Table 7. Abundances have been normalized to exclude blackbody percentages (-26.5% - 33%) [*Hamilton et al.,* 1997*; Feely and Christensen,* 1999*; Hamilton and Christensen,* 2000].

Contrary to measured mineralogy, plagioclase is the most abundant modeled mineral phase present in basalts, trachyandesites, and mafic trachytes. Plagioclase is not, however, present in peralkaline trachytes and rhyolites. All samples contain variable abundances of alkali feldspar, with basalts, trachyandesites, and mafic trachytes consisting of < 50 vol % and peralkaline trachytes and rhyolites containing > 50 vol %. Silica-rich glass is modeled in all three rhyolite samples at abundances ranging from 4-7 vol %. However, K_2O-silica glass, which was measured at high abundances in all rock

types, is not modeled in any samples. Orthopyroxene is modeled in all rock types except rhyolites, and clinopyroxene is present in all groups. Modeled pyroxene abundances are often significantly higher than measured values. Clinopyroxene and orthopyroxene abundances range from <1-23 vol % and from <1-31 vol %, respectively. Very low abundances (<1-6 vol %) of amphibole are modeled in all rock types, and olivine is present in all rock groups except for trachyandesites at abundances ranging from <1 to 4 vol %. Apatite is present in all but one of the samples that contain olivine and in a few samples where olivine is not modeled. Siderite is also modeled in almost all samples at abundances less than 6 vol %.

Uncertainties in individual modeled mineral abundances were determined by calculating 1σ standard deviations of the difference between mineral abundances as determined by electron microprobe and linear deconvolution techniques. Table 8 (top) shows the 1σ standard deviations of the differences between modeled and measured mineral abundances. Standard deviations range from 0.68 vol % (apatite) to 15.02 vol % (plagioclase) with an average standard deviation of 5.66 vol %. With the exception of alkali feldspar, plagioclase, and orthopyroxene, all standard deviations are less than 5 vol %. Mean absolute differences are similar to standard deviations, with values ranging from 0.45 vol % (apatite) to 18.15 vol % (plagioclase). All mean absolute errors are less than 6 vol %, with the exception of alkali feldspar and plagioclase.

Previous studies have calculated an absolute error of ± 5-10 vol% for modeled phase abundances, due mainly to contributions from instrument noise and precision [*Ramsey and Christensen,* 1998]. Traditional point counting methods typically have error of ± 5-10 vol% for major minerals and ~5 vol% for minor minerals. Much of the

uncertainty associated with traditional point counting is eliminated using the electron microprobe phase mapping technique employed in this study. With a relative precision of < 5 vol % [*Taylor et al.*, 1996], this technique is the most accurate method available for determining modal abundances, and also allows for modeled errors to be calculated for individual minerals, rather than as an average error for all mineral abundances.

Modeled mineralogies can be compared to measured mineralogies to determine overestimations and underestimations of deconvolved abundances and to identify possible missing endmember mineral phases. Electron microprobe (measured) and deconvolved (modeled) abundances for basalt, trachyandesite, trachyte, and rhyolite samples are shown in Figures 6a and 6b. Table 8 (top) lists errors modeled phase abundances. Errors for individual modeled minerals are 1σ standard deviation between measured and modeled abundances. Errors for measured modes relative to uncertainty associated with the phase mapping technique [*Taylor et al.*, 1986]. The solid diagonal line in Figures 6a and 6b represents a 1:1 measured to modeled ratio, while dashed diagonal lines establish the 10 vol % uncertainty field previously associated with modal mineralogies derived from linear deconvolution [*Ramsey and Christensen*, 1998]. Underestimation and overestimation of deconvolved modal abundances are relative to electron microprobe measured abundances.

Figure 6a shows that the majority of deconvolved mineral phases for basalts, trachyandesites, and mafic trachytes are within the 10 vol % error field. Two feldspar abundances fall outside of the 10 vol % uncertainty field by an additional 12-14 vol %. All plagioclase abundances in all basalt, trachyandesite, and mafic trachyte samples plot outside the 10 vol % uncertainty field by 7-27 vol %. Deconvolved and measured

mineral abundances for peralkaline trachytes and rhyolites are displayed on Figure 6b. Like basalts, trachyandesites, and mafic trachytes, most deconvolved mineral phases for peralkaline trachytes and rhyolites are within the 10 vol % error field. Only three deconvolved abundances, two feldspars and one quartz, fall outside of the 10 vol % uncertainty field. The quartz abundance falls outside the 10 vol % uncertainty field by only 3 vol %, whereas alkali feldspar abundances are outside the 10 vol % error field by 5-23 vol%. With the exception of plagioclase, most phase abundances are within the 10 vol % error field and are consistent with previously determined uncertainties for linear deconvolution [*Ramsey and Christensen,* 1998].

Silica-K_2O glass is measured in all alkali rock samples at abundances ranging from 6-58 vol%. However, the only glass endmember present in modeled modes is silica-rich glass (i.e., 99.9 wt % SiO_2). Trace abundances of silica glass are modeled in basalt 49005 (<1 vol %) and in all rhyolite samples at abundances ranging from 4-7 vol %. Although glass compositions vary widely between rock types, only three glass end-members are available in the current spectral library. The underestimation of silica-K_2O glass suggests that available glass end-members may not be representative of the composition or crystallinity of glasses measured using the electron microprobe. Representative analyses of glasses present in the Nandewar rocks, along with compositions of current glass end-members, are listed in Table 9. Compositions of glasses measured in the Nandewar rocks do not match available end-member compositions, as measured glass is significantly lower in silica and higher in aluminum and calcium than available spectral end-members. In fact, measured glass compositions are more similar to plagioclase endmember compositions, specifically labradorite. Visual

examination of analyzed glasses using backscatter electron (BSE) imaging indicates that glassy areas have been devitrified, which may explain the chemistry of Nandewar glasses. Areas identified as devitrified glass using the electron microprobe would likely have a spectrum similar to plagioclase, and therefore would model as plagioclase rather than as glass. This not only explains the absence of modeled silica-K_2O, but also accounts for high modeled abundances of plagioclase. This trend of high modeled plagioclase abundances corresponding to measured silica-K_2O glass is in fact present in the Nandewar samples, and is especially prominent in basalts and trachyandesites, rocks that typically contain higher abundances of plagioclase than trachytes and rhyolites. Assuming silica-K_2O glass was modeled as a plagioclase end-member, a more accurate indicator of measured plagioclase abundances can be produced by combining measured glass abundances with measured plagioclase abundances. For example, microprobe phase mapping indicates that basalt 49000 contains 36 vol % plagioclase and 25 vol % glass. In the same sample, plagioclase models at 53 vol %. Combing measured glass and plagioclase abundances results in a total of 61 vol %, which more accurately matches modeled plagioclase abundances. This same trend is present in all samples, as combining abundances of measured plagioclase and silica-K_2O glass results in total abundances that equal or exceed the amount of modeled plagioclase.

4.3. Derived Chemistry

Derived chemistry varies slightly as a function of the end-members selected. In this section, we address how well derived alkali and plagioclase feldspar, pyroxene, and bulk-rock chemistries compare to laboratory-measured values, in order to examine the accuracy of mineral compositions derived from linear deconvolution.

4.3.1. Alkali feldspar compositions

Alkali feldspar endmembers are modeled in all basalt, trachyandesite, trachyte, and rhyolite samples. Figure 7 shows deconvolved and measured alkali feldspar and plagioclase compositions plotted on an An-Ab-Or ternary diagram for feldspars, which illustrates all compositional fields for both the alkali feldspar (albite to orthoclase) and plagioclase feldspar (albite to anorthite) solid solution series. The unlabeled field represents feldspar compositions that do not occur in nature.

Deconvolved alkali feldspar compositions in basalts, trachyandesites, and mafic trachytes were modeled using varying abundances of three end-members: anorthoclase, microcline, and sanidine. Deconvolved compositions extend over a small compositional range within the sanidine field. Modeled feldspar compositions in all basalt and trachyandesite samples are either Or_{69} or Or_{71}, while modeled compositions in mafic trachytes range from Or_{60} to Or_{70}. Feldspar compositions in peralkaline trachytes and rhyolites, which were modeled using a larger number of feldspar end-members, extend over a wider compositional range (Or_{20-48}) and are more calcium-rich, plotting within the anorthoclase ($< Or_{37}$) field and sanidine ($> Or_{37}$) fields.

Figure 7 compares deconvolved feldspar compositions to compositions measured in basalts, trachyandesites, trachytes, and rhyolites [*Stolz,* 1986]. With compositions ranging from ~Or_{10-50}, measured alkali feldspar chemistries in basalts, trachyandesites, and mafic trachytes fall into the anorthoclase and sanidine fields. All deconvolved basalt, trachyandesite, and mafic trachyte feldspar compositions are also sanidine. However, modeled sanidine compositions (Or_{60-70}) are significantly more potassium-rich than measured compositions and plot outside of the range of measured compositions (Figure

7). Measured feldspar chemistries in peralkaline trachytes and rhyolites occur over a small compositional range (Or_{26-49}), with the majority of analyses concentrated between Or_{34} and Or_{42} [*Stolz*, 1986]. Modeled feldspar compositions in peralkaline trachytes and rhyolites (Or_{20-48}) occur over the same compositional range. However, because deconvolved feldspar compositions in peralkaline trachytes and rhyolites have a higher mol % An component than measured compositions, most modeled compositions plot slightly outside of the range of measured compositions (Figure 7). Modeled anorthoclase compositions are more calcic than measured compositions because modeled compositions were produced by combining all modeled feldspar end-members, including plagioclase end-members, such as oligoclase and andesine. The inclusion of these Ca-rich end-members results in modeled anorthoclase compositions with higher calcium contents than measured compositions.

Sanidine compositions in basalts, trachyandesites, and peralkaline trachytes model higher in potassium than measured compositions as a result of available end-member compositions. The composition of the sanidine spectral end-member (Or_{69}) indicates that it belongs to the high albite - high sanidine series. This series represents complete solid solution, and all K-rich members (sanidine) are monoclinic. The range of measured anorthoclase compositions are, however, indicative of the high albite - sanidine series. In this series, feldspar compositions are unmixed, and anorthoclase and sanidine are distinguished by a change in symmetry from triclinic to monoclinic, which occurs at Or_{37}. Because the only sanidine end-member available is from the high sanidine - high albite series, all modeled sanidine will have the composition of this sanidine end-member,

which in this case is Or_{69}. The presence of sanidine is therefore being modeled correctly, however the composition cannot be accurately modeled by the available end-member.

4.3.2. Plagioclase feldspar compositions

As multiple plagioclase endmembers were modeled in each rock sample, an average plagioclase composition was determined by combining the contribution of each endmember. Plagioclase end-members modeled in peralkaline trachytes and rhyolites were combined with modeled alkali feldspar end-members to reproduce the single feldspar composition measured in these rock types. Feldspar compositions are discussed in section 4.3.1. Deconvolved and measured plagioclase compositions are plotted along with alkali feldspar compositions on an An-Ab-Or ternary diagram for feldspars in Figure 7. Deconvolved and measured plagioclase compositions in basalts, trachyandesites, and mafic trachytes range from An_{32}-An_{51}, falling primarily into the andesine field. Overall, deconvolved plagioclase compositions fall within the range of measured compositions [*Stolz*, 1986].

Figure 7 compares deconvolved plagioclase compositions to compositions measured in basalt, trachyandesite, and mafic trachyte samples [*Stolz*, 1986]. Measured plagioclase compositions extend over a wider compositionally range than modeled compositions, plotting within the andesine and labradorite fields (~An_{30-70}). The wider range of measured plagioclase compositions is not unexpected, as naturally occurring plagioclase is often zoned, exhibiting a wide range of compositions within a single phenocryst. Deconvolved chemistries, however, represent only an average plagioclase composition within an individual rock sample. All deconvolved plagioclase compositions plot well within the range of measured chemistries, suggesting that the

average plagioclase composition of basalts, trachyandesites, and mafic trachytes is andesine.

4.3.3. Pyroxene compositions

Deconvolved and measured pyroxene compositions for basalts, trachyandesites, trachytes, and rhyolites are plotted on a pyroxene quadrilateral for the diopside (Di)-enstantite (En)- hedenbergite (Hd)- ferrosilite (Fs) system in Figures 8a and 8b. Deconvolved compositions were determined using either a single pyroxene end-member (e.g. enstatite NMNH-120414-1) or by combining two or more pyroxene end-members (e.g. enstatite NMNH-120414-1 plus enstatite NMNH-119793) to produce an intermediate composition. In most samples, both orthopyroxene and clinopyroxene end-members were modeled. These endmembers were treated as separate pyroxene phases and were not combined with one another to form an intermediate composition. Measured pyroxene compositions represent an average composition in a given rock sample. As a result, measured pyroxene compositions are limited and do not represent the entire range of compositions possible in a given sample.

Figure 8a shows that deconvolved pyroxene compositions accurately reproduce measured phases in basalts and trachyandesites. Both clinopyroxene and orthopyroxene are present in basalt and trachyandesite samples [*Abbott*, 1969; *Stolz*, 1986] and both phases are accurately modeled in all but one of the four basalt and trachyandesite samples. In basalt sample 49000, a single clinopyroxene end-member is modeled with a composition that almost perfectly reproduces measured clinopyroxene compositions in the same sample. Both clinopyroxene and orthopyroxene are modeled in basalt sample 49005 and in both trachyandesites. Modeled clinopyroxene and orthopyroxene

compositions accurately reproduce measured compositions in all samples except for basalt 49005, in which modeled clinopyroxene compositions are slightly more Fe-rich than measured compositions. Orthopyroxene was not measured in sample 49005, although a small abundance (<1 wt %) of orthopyroxene was modeled. The modeled orthopyroxene composition matches orthopyroxene compositions present in several other trachyandesite samples. This abundance, however, is below the detection limits for the linear deconvolution technique and is therefore not reliable.

Figure 8b indicates that modeled pyroxene compositions in trachytes and rhyolites do not reproduce measured compositions as well as those in the basalts and trachyandesites. Measured pyroxene compositions in Nandewar trachytes extend across the diopside and hedenbergite fields, with most analyses plotting as hedenbergite [*Stolz*, 1986]. Clinopyroxene, however, does not model in any of the trachyte samples examined in this study. Instead, enstatite models at abundances ranging from 4-31 vol % in three of the four trachytes. Pyroxene is not modeled in trachyte sample 15802. Low pyroxene abundances are modeled in rhyolites, which is expected in this rock type. Orthopyroxene is not modeled in any of the rhyolite samples, and clinopyroxene models in two samples at abundances of only <1 and 1 wt %. Because rhyolites do not generally contain mafic minerals, measured pyroxene compositions in this rock type are limited [*Stolz*, 1986]. As a result, it is difficult to make a direct comparison with measured compositions. However, modeled clinopyroxene compositions in rhyolites are similar to compositions measured in trachytes, although they are slightly more calcic.

The poor modeling of pyroxene in trachyte samples may be explained by a combination of factors. Abundances of orthopyroxene in sample 49083 are below the

detection limits of the linear deconvolution technique [*Ramsey and Christensen*, 1998; *Feely and Christensen*, 1999; H*amilton and Christensen*, 2000]. High pyroxene abundances modeled in trachyte 49098 are not believed to be reliable either, as the RMS error in this sample is extremely high (0.613). The occurrence of orthopyroxene in sample 15800 is more difficult to explain, as abundances are above detection limits and the RMS error indicates that the modeled spectrum is a good fit with the measured spectrum. Small deviations between modeled and measured spectra do occur in regions where at pyroxene absorption features are prominent (i.e. 1200-800 cm^{-1} and 600-400 cm^{-1}). Modal abundances of orthopyroxene may be inflated as the result of redistribution of other poorly modeled phases. Amphibole, for example, was measured in sample 15800 at 7 vol %, but failed to appear in modeled mineralogy. This phase would have been redistributed throughout other phases by the linear deconvolution algorithm, resulting in slightly elevated abundances for one or more phases.

4.3.4. Derived bulk rock chemistry

Figure 9 shows measured versus derived oxide abundances for all basalt, trachyandesite, trachyte, and rhyolite samples. Apatite and siderite end-members were not included in derived bulk chemistry calculations, as chemical data is not available for these end-members. Both minerals were measured at low abundances (< 3 vol %) and modeled at abundances below the detection limit for the linear deconvolution method [*Ramsey and Christensen*, 1998]. Therefore, the exclusion of these phases should not adversely affect derived bulk chemistries. Mean absolute uncertainties, mean relative uncertainties, and 1σ standard deviations for each oxide are listed in Table 8 (bottom).

Overall, derived oxide abundances correlate well with measured values, with

mean absolute differences ranging from 0.17 wt % (MnO) to 3.76 wt % (SiO2). Silica is the most poorly modeled, with absolute differences ranging from -5.61 wt % (underestimation) to +8.22 wt % (overestimation). Alkali oxides (Na_2O and K_2O) are well modeled, with absolute errors ranging from -1.78 to 2.37 wt % for K_2O and from -3.79 to 0.80 wt % for Na_2O. MnO has the lowest mean absolute error of all measured oxides, with absolute differences of only -0.09 to +0.78 wt %. All but one derived abundances of Al_2O_3 are overestimated (-0.07 to +2.92 wt %), while all FeO abundances are underestimated (-0.60 to -6.71 wt %). All absolute errors for CaO abundances are overestimated, with errors ranging from +0.37 to +4.51 wt %. Absolute errors range for TiO_2 and MgO range from -2.48 to +0.04 and from +0.12 to +9.72, respectively.

The absolute errors between measured and derived oxide abundances suggest that most oxides are well modeled. However, silica, the most abundant oxide in alkalic rocks, is poorly modeled, especially in basalts, where silica oxide abundances are overestimated by 6.63 and 8.22 wt %. In peralkaline trachytes and rhyolites, silica abundances are underestimated by an average 3.78 wt %. Poor modeling of silica abundances is likely due to the exclusion of Fe-oxide end-members such as hematite and ilmenite, which were measured at abundances ranging from 2 to 4 wt % in basalts, trachyandesite, and mafic trachytes. At such low abundances, the exclusion of these endmembers should not have a significant negative overall effect on derived chemistry. However, because Fe-oxide minerals typically have extremely low silica abundances (<1 wt % SiO_2), exclusion of these oxide minerals could have produced the increased derived silica oxides in basalts, trachyandesites, and mafic trachytes. Underestimation of silica oxides in peralkaline trachytes and rhyolites is likely the result of modeled silica phase abundances (e.g.,

quartz and silica glass) being underestimated by linear deconvolution. The exclusion of Fe-oxide end-members is also responsible for the poor modeling of FeO, which is underestimated in all samples. Fe-oxide abundances are particularly underestimated in basalts, trachyandesites, and mafic trachytes, by an average of 5.06 wt %. Because Fe-oxide minerals consist primarily of FeO and Fe_2O_3, the exclusion of these mineral phases would have a significant negative affect on derived FeO oxides.

5. VOLCANIC ROCK CLASSIFICATION

Volcanic rocks are typically classified using classification schemes based on bulk rock chemistry [e.g., *Le Bas et al.*, 1986]. Because derived chemistry is the most model dependent data set in this study, if samples are accurately classified using this method, less model-dependant results, such as modeled mineralogy, can be validated.

5.1. Deconvolved Modal Mineralogy

Modal mineralogy was examined using the IUGS classification of volcanic rocks [*LeMaitre*, 1989] to access the accuracy of using deconvolved mineralogies to distinguish alkalic rock types. Figure 10 shows modal mineral abundances of quartz, alkali feldspar, and plagioclase (renormalized to 100 vol %) superimposed on a quartz-alkali-plagioclase (QAP) diagram. Using the IUGS classification scheme, five of eleven samples are correctly identified. Both basalt samples plot within the andesite/basalt field, which is defined as having greater than 65% plagioclase and less than 20% quartz. Of the Nandewar trachyandesites, sample 49074 is correctly classified, while sample 49012 plots incorrectly in the andesite/basalt field. Modeled plagioclase abundances place both mafic trachytes within the trachyandesite field, while peralkaline trachytes, which modeled 100% alkali feldspar, are identified as alkali trachytes (> 90% alkali, < 5% quartz). The alkali rhyolite field is characterized by quartz abundances ranging from 20-60% and > 90% alkali feldspar. Because of modeled quartz abundances less than 20%, all rhyolite samples are incorrectly classified as quartz alkali trachytes.

5.2. Derived Mineral Chemistry

The suite of Nandewar alkalic rocks was also classified using a scheme developed by *Irvine and Baragar* [1971], which uses normative plagioclase compositions

(mol % An = 100An/(An+Ab)) and normative color index (modal olivine + clinopyroxene + orthopyroxene + amphibole) to distinguish between alkaline rock compositions (Figure 11). This classification system defines alkali basalt, trachybasalt, tristanite, trachyte, and rhyolite with decreasing color index and decreasing normative plagioclase. Trachyandesites are not distinguished using this classification scheme. The 1σ standard deviation for normative color index is the root-mean-square of standard deviations for modeled olivine, pyroxene, and amphibole (Table 8, top). Standard deviation for mol % An cannot be calculated because measured plagioclase compositions are not available for the exact samples examined in this study. Plagioclase compositions referenced in section 4.3.2. were determined from the analyses of Nandewar volcano samples that were not used in this study. Therefore, a direct comparison needed to determine a standard deviation cannot be made. Using the *Irvine and Baragar* classification system, all basalts and rhyolites are classified correctly. However, only one trachyte sample is correctly classified, while the remaining three trachytes are misclassified as trachybasalts or tristanites. When error bars are considered, most samples extend into surrounding classifications fields when error bars are applied.

5.3. Derived Bulk Rock Chemistry

Derived silica versus alkalis (Na_2O+K_2O) of the Nandewar volcanic rock samples are superimposed on the chemical classification scheme for volcanic rocks [*Le Bas et al.*, 1986] in Figure 12. All samples are accurately classified as alkaline, and 8 of 11 samples plot within correct chemical classification fields. Derived alkali oxide abundances reproduce measured abundances well. However, silica content is overestimated in most basalt and trachyandesites, resulting in incorrect classifications of these rock types. Silica

abundances are slightly underestimated in trachytes and rhyolites, though it does not adversely affect the classification of most of these samples. Basalt 49000, overestimated in silica by 6.6 wt %, plots in the basaltic andesite field, while trachybasalt 49005, overestimated by 8.2 wt %, plots on the boundary between basaltic trachyandesite and trachyandesite fields. Basaltic trachyandesite 49012 is accurately classified as a basaltic trachyandesite; however, errors bars do extend this sample into the trachyandesite field, making the classification slightly obscure. Sample 49074 is accurately classified as a trachyandesite, although derived alkalis are slightly lower than those measured. Of the four trachyte samples, both mafic trachytes and one peralkaline trachyte (15802) plot in the trachyte field. Peralkaline trachyte 49098 is highly underestimated in alkalis and is inaccurately classified as a trachyandesite. All rhyolite samples are slightly underestimated in alkali and silica abundances, but are classified very well using the chemical classification system. Sample 15807 falls on the chemical boundary between trachyte and rhyolite, and samples 49130 and 15806 both plot firmly in the rhyolite field.

A second chemical classification system by *Cox et al.* [1980] also relies on silica and alkali oxides to distinguish between volcanic rock types. Although very similar to the Le Bas classification scheme, some variation in terminology exists, and classification fields are defined using slightly different ranges of alkali and silica oxide abundances. Figure 13 shows derived silica and alkali oxides superimposed on the *Cox et al.* [1980] classification scheme. Overall, there is little difference between those classifications obtained using *Le Bas et al.* [1986] and *Cox et al.* [1980]. Both basalt samples are misclassified, with sample 49000 plotting in the basaltic andesite field and sample 49005 in the trachyandesite field. Both trachyandesites, two of the four trachytes, and all three

rhyolites are classified correctly. The remaining two trachytes, which were also misclassified using *Le Bas et al.* [1986], are classified as trachyandesites. Using the *Cox et al.* [1980] classification scheme, 7 samples are classified correctly.

5.4. Summary of Classifications

Table 10 summarizes results for each classification scheme to determine the accuracy of using each method (i.e. modal mineralogy, derived mineral chemistry, and derived chemistry) to distinguish alkalic volcanic rocks. Samples are divided into six groups based on measured chemistry: basalts, trachybasalts, basaltic trachyandesites, trachyandesites, trachytes, and rhyolites. In classification schemes other than derived bulk rock chemistry, trachybasalt sample 49005 is grouped with basalts, while basaltic trachyandesite sample 49012 is referred to as a trachyandesite. For each classification scheme, a sample is assigned a letter (or letters) representing the type of rock it is classified as (e.g. B for basalts, TA for trachyandesites). Letters in parenthesis represent changes in classification due to the error bars that extend into other classification fields.

Basalts are best classified using derived mineral chemistry, whereas trachyandesites and trachytes are most accurately classified using derived bulk-rock chemistry. Either scheme can be used to classify rhyolites, as both derived mineral and bulk-rock chemistry correctly identified all three rhyolite samples. No single classification scheme can identify all basalts, trachyandesites, trachytes, and rhyolites. However, all rock types can be accurately classified using a combination of the mineral and bulk-rock chemistry classification systems.

6. Applications to Martian Remote Sensing

6.1. Deconvolution of Rock Compositions at TES Resolution

The spectral sampling of TES can be selected at 5 or 10 cm^{-1} [*Christensen et al.*, 1992]. Laboratory rock spectra were resampled to the lowest TES resolution to provide a more adequate representation of data collected from martian orbit. However, these data do not provide an exact comparison, as laboratory-collected spectra have a higher signal-to-noise-ratio (SNR) than TES spectra and do not contain any significant atmospheric components that must be removed. Although the effects of SNR on spectral deconvolution have not been addressed, it is possible that the lower SNR of the TES instrument may be a significant factor in the accuracy of model-derived data. As a result, a future assessment of SNR in linear deconvolution may be warranted. A ~10-15 vol % uncertainty [*Christensen et al.*, 2000a; *Bandfield et al.*, 2000a] of modal mineralogies is applied to TES surface spectra as a result of instrumental uncertainties [*Christensen et al.*, 2000a] and errors associated with atmospheric corrections [*Smith et al.*, 2000; *Bandfield et al*, 2000]. In this section, modeled spectra, modeled mineralogies, and derived chemistries at 10 cm^{-1} resolution spectra are examined to determine whether adequate results can be obtained at a resolution comparable to that of TES spectra obtained from Mars orbit.

Overall, there are few discrepancies between modeled spectra, modal mineralogies, and bulk-rock chemistries determined by deconvolution of laboratory spectra at a sampling of 2 cm^{-1} and 10 cm^{-1}. Measured and modeled spectra of basalt, trachyandesites, trachytes, and rhyolites at TES resolution are shown in Figure 14. These spectra can be compared to laboratory resolution spectra in Figure 5. There is very little

difference in the quality of fits at a reduced spectral sampling. In fact, RMS errors associated with linear deconvolutions of TES resolution spectra are lower than errors of spectra at laboratory resolution, with errors ranging from 0.263 to 0.493. The most significant improvement in goodness of fit occurs in sample 49098, which improves from 0.613 to 0.339 at 10 cm^{-1} spectral sampling. The same spectral misfits present in laboratory resolution spectra are also visible in TES resolution spectra; however, no additional misfits are present at lower resolution. It is unclear why goodness of fit improves at 10 cm^{-1} sampling, although it may be a result of oversampling the characteristic width of absorption bands used to model the spectra [*J. Moersch*, personal comm.].

Deconvolved modal mineralogy at 10 cm^{-1} is shown in Table 11. Modes have been normalized to remove blackbody components (-26.9 to 21.8%). Errors associated with linear deconvolution derived modal mineralogy at 10 cm^{-1} are calculated in the same way as the 2 cm^{-1} results (See section 4.2.). Errors for mineralogy and chemistry are listed in Table 12. The 1σ standard deviation for mineralogies modeled at 10 cm^{-1} spectral sampling range from 1.15 vol % to 12.85 vol %, with a mean standard deviation of 4.67 vol %. These results are similar to those obtained at 2 cm^{-1}, suggesting that linear deconvolution at lower spectral sampling does not adversely affect the uncertainty associated with model-derived modal mineralogy.

Figure 15 compares deconvolved mineralogies at spectral samplings of 2 cm^{-1} and 10 cm^{-1}. There are only minor differences between modal abundances obtained from deconvolution of spectra at 2 cm^{-1} and 10 cm^{-1} spectral sampling. Most abundances do not differ by more than 10 vol %, while some phases, such as quartz, olivine, and glass,

have absolute differences less than 5 vol %. Phases with errors greater than 10 vol % include pyroxene, amphibole, and plagioclase, which together have only four data points that plot outside of the 10 vol % uncertainty range (Figure 15). Absolute differences in plagioclase (13 vol %) and orthopyroxene (14 vol %) are only slightly outside of the 10 vol % uncertainty range in trachyte 15800 and trachyandesite 49012, respectively. The largest absolute errors occur in trachyte sample 49098, where orthopyroxene abundances modeled at 2 cm^{-1} (35 vol %) decrease to 3% at 10 cm^{-1}. This decrease in pyroxene is compensated for by a 19% increase in amphibole. Linear deconvolution of sample 49098 at laboratory resolution (2 cm^{-1}) produced a very high RMS error (0.613), suggesting that this model-derived mineralogy may contain significant inaccuracies. However, the RMS error for linear deconvolution at 10 cm^{-1} spectral sampling was significantly lower (0.339). This indicates that modal mineralogy determined at 10 cm^{-1} is more indicative of actual mineralogy than that determined at 2 cm^{-1}. With such a substantial difference between RMS errors at 2 cm^{-1} and 10 cm^{-1}, these large absolute errors are expected. With the exception of these few pyroxene, amphibole, and plagioclase points, results from deconvolutions performed at 2 cm^{-1} and 10 cm^{-1} spectral sampling are very similar, suggesting that derived mineralogies determined at a reduced spectral sampling are comparable to those obtained at higher spectral resolutions.

Bulk chemistries derived at 10 cm^{-1} spectral sampling also compare well with those derived at 2 cm^{-1} sampling. Derived oxide abundances at 2 cm^{-1} and 10 cm^{-1} are compared in Figure 16; errors associated with bulk chemistry are listed in Table 12. Like errors at 2 cm^{-1}, the worst uncertainties at 10 cm^{-1} are associated with FeO and SiO_2, while the lowest mean absolute difference is observed in MnO. Few changes exist

between the remaining oxides at 2 cm^{-1} and 10 cm^{-1}, and those that do exist are insignificant, as these oxides are not used in any classification schemes.

Oxides most essential in alkalic rock classification are silica and alkalis. Average standard deviations and absolute uncertainties of silica and alkali abundances at 10 cm^{-1} spectral sampling are comparable to those at 2 cm^{-1}. However, individual silica and alkali abundances are slightly higher at 10 cm^{-1} spectral sampling. Elevated derived alkali oxide abundances at 10 cm^{-1} spectral sampling may be the result of higher model-derived amphibole abundances. The trend of silica overestimation in basalts and trachyandesites is also apparent at 10 cm^{-1} spectral sampling, as silica oxide abundances are overestimated in basalts, trachyandesites, and mafic trachytes (3.2-6.8 wt %) and underestimated peralkaline trachytes and rhyolites (1.17-4.61 wt %). Differences in alkali oxide abundances at 2 cm^{-1} and 10 cm^{-1} only affect chemical classification of the trachyandesite samples.

6.2. Volcanic Rock Classification at TES Resolution

To examine the accuracy of volcanic rock classification at decreased spectral resolution, basalts, trachyandesites, trachytes, and rhyolites were classified using the most successful classification schemes discussed in section 5.4. Samples were first classified using the *Irvine and Baragar* [1971] system (Figure 17), which correctly identified 6 of 9 samples at 2 cm^{-1} spectral sampling. The 1σ standard deviation for normative color index is the root-mean-square of standard deviations for modal olivine, pyroxene, and amphibole modeled at 10 cm^{-1} sampling (Table 12). Standard deviation for mol % An cannot be calculated, as measured plagioclase compositions are not available for the exact samples examined in this study. (See section 5.2. for discussion.) Classifications at

10 cm^{-1} spectral sampling are nearly identical to those obtained at 2 cm^{-1} spectral sampling. All basalts and rhyolites are again classified correctly. Three trachytes are again misclassified, this time as tristanites, and one trachyte falls on the boundary between tristanite and trachyte. Trachyandesite samples were not classified, as there is no classification field for trachyandesites established by *Irvine and Baragar*. Overall, 6 of 9 samples are identified correctly, consistent with classifications at 2 cm^{-1} sampling.

Alkalic rock samples were also classified using derived silica versus alkali oxides at 10 cm^{-1} spectral sampling. These classifications, along with classifications determined at 2 cm^{-1} spectral sampling, are superimposed on the *Le Bas et al.* [1986] diagram in Figure 18. Most samples remain virtually unchanged from 2 cm^{-1} to 10 cm^{-1} spectral sampling. All basalt, trachyte, and rhyolite samples retain their 2 cm^{-1} classification at a lower spectral resolution. However, both trachyandesite are classified differently at 10 cm^{-1} as a result of increased silica and alkali oxide abundances. At 10 cm^{-1} spectral resolution, trachyandesite 49012 becomes correctly classified, while trachyandesite 49074 becomes incorrectly classified as a trachyte. Overall, results at 10 cm^{-1} spectral sampling are comparable to those at 2 cm^{-1}, with 8 of 11 samples being classified correctly at both resolutions. These results indicate that TES-resolution data can be successfully applied to alkalic rock classification.

6.3. Deconvolution of TES Surface Spectra

TES data have identified two distinct compositions on the surface of Mars, the first being a basalt [Christensen et al., 2000a; Bandfield et al., 2000a] and the second being either andesite [Bandfield et al., 2000a] or partially weathered basalt [Wyatt and McSween, 2002]. Surface type 1 is confined primarily to the southern highlands,

whereas surface type 2 is found mainly in the northern lowlands [*Bandfield et al.*, 2000a; *Wyatt et al.*, 2004]. Deconvolutions used to identify each of these surface types were performed using mineral end-members different from those used in this study, and therefore may not be directly comparable. However, we wanted to deconvolve both TES surface types using our end-member set, which was tailored for alkaline rocks, to determine whether our end-member set can also correctly identify known subalkaline rock compositions. In doing so, we also address the variability associated with using different end-member sets to deconvolve the same unknown spectrum.

Modal mineralogies of the two martian surface types were determined using the end-member set used in the deconvolutions of the Nandewar alkalic rock samples, which consist primarily of feldspars, pyroxenes, and amphiboles, and contain several spectral end-members formerly not available. Table 13 lists model-derived modal mineralogies of the two TES surface types as determined using our spectral end-member set, along with modal mineralogies previously determined by *Christensen et al.* [2000a], *Bandfield et al.* [2000a], and *Hamilton et al.* [2001] for comparison. Our modeled spectra are compared to spectra from *Bandfield et al.* [2000a] in Figure 19.

Using our alkalic rock end-member set, deconvolved modal mineralogies of surface type 1 resemble those of derived by *Christensen et al.* [2000a], while deconvolutions of surface type 2 closely match those determined by *Bandfield et al.* [2000a]. Deconvolution results in *Christensen et al.* [2000a] are for the spectrum of a basaltic component identified at Cimmeria Terra. This spectrum is similar, although not identical, to the *Bandfield et al.* [2000a] surface type 1 spectrum. However, the surface type 1 spectrum of *Bandfield et al.* [2000a] does include spectra from Cimmeria Terra.

The most abundant phases modeled in the *Christensen et al.* [2000a] Cimmeria Terra spectrum are feldspar and clinopyroxene. Our model-derived feldspar and clinopyroxene abundances correspond with those of Christensen et al. [2000a] very nicely, differing only by 10 vol % and 5 vol %, respectively. Olivine is also present in both deconvolutions at abundances differing by only 6 vol %. The largest discrepancy is between the two models is the absence of sheet silicates and the presence of Na-pyroxene in our deconvolved surface type 1 mineralogy. Our model-determined mineralogy also contains small abundances of amphibole and siderite, however both are below the detection limits of TES [Christensen et al, 2000a; Bandfield et al., 2000a].

Deconvolved mineralogies of surface type 2 closely resemble those from *Bandfield et al.* [2000a]. With the exception of sheet silicates and Na-pyroxene, phase abundances modeled in both deconvolutions do not differ by more than 8 vol %. Like *Bandfield et al.* [2000a], the most abundant phases modeled in our deconvolutions are feldspar and glass (30 and 17 vol %, respectively). Clinopyroxene, amphibole, and olivine also model at comparable abundances in both deconvolutions. Phases modeled in our deconvolutions that are not present in *Bandfield et al.* [2000a] deconvolutions include glass (2 vol %), Na-pyroxene (15 vol %), and siderite (6 vol %). Both glass and siderite are below detection limits of TES as stated by *Christensen et al.* [2000a] and *Bandfield et al.* [2000a]. Because Na-pyroxene is at the lower detection limit of 15 vol %, it is difficult to establish if it is indeed present. As with the comparison of surface type 1 deconvolutions, the most significant deviation between each modeled surface type 2 spectra is the absence of sheet silicates in our deconvolutions, which is compensated for by the presence of Na-pyroxene. This is easily explained in both instances, as sheet

silicate end-members were not used in our deconvolutions, and therefore could be modeled. The variations between modeled abundances in both surface types are the result of differences between the end-members used.

Bulk rock chemistries of each martian surface type were derived from modeled mineralogies, and derived silica and alkali oxides were plotted on the classification diagram of *Le Bas et al.* [1986] to determine the classification of each surface type based on our end-member set (Figure 20). Error bars represent the 1σ standard deviation of derived oxides at 10 cm^{-1} spectral sampling (Table 12). Using our end-members, surface type 1 is classified as a trachybasalt and surface type 2 is classified as an andesite. With the addition of error bars, surface type 1 extends into the basaltic andesite field, plotting near previously modeled surface type 1 chemistries. The classification of surface type 2 is made more uncertain by the addition of error bars, which extend into both the trachyandesite and dacite fields. Our surface type 1 and 2 classifications differ from those determined in previous studies [*Christensen et al.*, 2000a; *Bandfield et al.*, 2000a; *Hamilton et al.*, 2001] as a result of higher modeled alkali oxide abundances. This trend of overestimation of alkali oxides is also present in terrestrial basalts and trachyandesites examined in this study by ~0.5-2 wt %. A comparable overestimation of alkali oxides in our surface type 1 and 2 chemistries would not alter the classification of surface type 2. However, an alkali oxide overestimation > 0.5 wt % would result in the reclassification of surface type 1 as basaltic andesite. Overestimated alkali oxides may explain the classification of surface type 1 as a basaltic trachyandesite rather than a basaltic andesite. However, it is also possible that martian surface compositions are indeed more alkali-rich than previously thought, as previous results have relied on spectral end-member sets

tailored for subalkaline rock compositions [*Christensen et al.,* 2000a; *Bandfield et al.*, 2000a; *Hamilton et al.*, 2001]. Our results do not suggest that martian surface type 1 has been incorrectly identified, but rather indicate that an additional degree of uncertainty exists in the interpretation of TES-derived martian surface compositions.

7. CONCLUSIONS

1. Linear deconvolution of thermal emission spectra can successfully determine modal mineralogy and derive bulk chemistry of basalts, trachyandesites, trachytes, and rhyolites.

2. Comparison of modal mineralogies measured using electron microprobe phase mapping and of those derived from linear deconvolution indicate that the majority of phases are modeled within 10% vol error of measured phases. Large discrepancies, however, are present in silica-K_2O glass and plagioclase.

3. Glasses in the Nandewar rock suite are devitrified and have compositions similar to plagioclase. These glasses are not represented by available glass end-members and are modeled instead by plagioclase end-members. Modeled plagioclase abundances consist of both actual plagioclase and devitrified glass, explaining the absence of silica-K_2O glass and the presence of high abundances of plagioclase in model-derived modes.

4. Bulk-rock chemistries of alkalic rocks can be derived from modal mineralogies by combining the compositions of modeled end-members (wt % oxides) in proportion to their abundance within a sample (recalculated to wt %). Most oxides model well compared to relative to measured values. 1σ standard deviations range from 0.23 to 2.80 wt %. Modeled SiO_2 and FeO model poorly as the result of excluding Fe-oxide mineral phase from the end-member set.

5. Modeled mineralogies and derived chemistries of alkalic rocks can be applied to several different volcanic rock classification schemes to successfully distinguish between basalts, trachyandesites, trachytes, and rhyolites. No one classification scheme can accurately classify all alkalic rock samples. However, using a combination of the derived

mineral chemistry and derived bulk chemistry schemes, the majority (> 90%) of alkalic rocks samples are classified correctly.

6. Results of linear deconvolution of thermal emission spectra at TES instrument resolution are comparable to those obtained at laboratory resolution. Modeled spectra are comparable at both resolutions. Modeled mineralogies at 2 cm^{-1} and 10 cm^{-1} are very similar and generally do not differ by more than 10 vol %. Derived oxide abundances obtained at lower spectral resolution are also similar to those obtained at higher spectra sampling. Silica is once again poorly modeled, displaying trends in over- and under-estimation of silica abundance identical to those at seen 2 cm^{-1} resolution.

7. Modeled mineralogies and derived chemistries at lower spectral resolution can also be applied successfully to volcanic rock classification schemes. The same number of samples is classified correctly at 10 cm^{-1} spectral sampling using derived mineral and bulk-rock chemistry.

8. Deconvolution of martian surface spectra using an end-member set tailored for alkalic rocks produces modal mineralogies similar to those obtained in previous studies [*Christensen et al.*, 2000a; *Bandfield et al.*, 2000a]. Each mode represents a distinct lithology.

9. Bulk rock chemistries of the Martian surface spectra derived using our alkalic end-member set classify surface type 2 as a basaltic andesite. However, surface type 1 is classified as a trachybasalt, due mainly to overestimation of alkali oxides. This suggests an additional degree of uncertainty must be considered when classifying martian surface components.

REFERENCES

Abbott, M.J. (1969) Petrology of the Nandewar Volcano, N.S.W., Australia: *Contr. Mineral. and Petrol., 20*, 115-134.

Bandfield, J.L., P.R. Christensen, and M.D. Smith (2000), Spectral dataset factor analysis and endmember recovery: Application to analysis of martian atmospheric particulates, *J. Geophys. Res., 105*, 9573-9587.

Bandfield, J.L., V.E Hamilton, and P.R. Christensen (2000a), A global view of martian surface composition from MGS-TES: *Science, 287*, 1626-1630.

Christensen, P.R. et al. (1992) The Thermal Emission Spectrometer Experiment: Mars Observer Mission, *J. Geophys. Res., 97*, 7719-7734.

Christensen, P.R. and S. Harrison (1993), Thermal infrared emission spectroscopy of natural surfaces: Application to desert varnish coatings on rocks, *J. Geophys. Res., 98*, 19,819-19,834.

Christensen, P.R., J.L. Bandfield, V.E. Hamilton, D.A. Howard, M.D. Lane, J.L. Piateck, S.W. Ruff, and W.L. Stefanov (2000), A thermal emission spectral library of rock forming minerals, *J. Geophys. Res., 105*, 9735-9739.

Christensen, P.R., J.L. Bandfield, M.D. Smith, V.E. Hamilton, and R.N. Clark (2000a) Identification of a basaltic component on the martian surface from Thermal Emission Spectrometer data, *J. Geopys. Res., 105*, 9609-9621.

Christensen, P.R. et al., (2000b) Detection of crystalline hematite mineralization on Mars by the Thermal Emission Spectrometer: Evidence for near surface water, *J. Geophys. Res., 105*, 9632-9642.

Christensen, P.R., et al. (2001) The Mars Global Surveyor Thermal Emission Spectrometer experiment: Investigations descriptions and surface science results, *J. Geophys. Res., 106*, 23,823-23,871.

Coombs, D.S. and J.F.G. Wilkinson (1969) Lineages and fractionation trends in undersaturated volcanic rocks from the East Otago volcanic province (New Zealand) and related rocks, *J. Petrology, 10*, 440-501.

Cox, K.G., J.D. Bell, R.J. Pankhurst (1980), The Interpretation of Igneous Rocks, 450 pp., G. Allen and Unwin, London.

Feely, K.C. and P.R. Christensen (1999), Quantitative compositional analyses using thermal emission spectroscopy: Application to igneous and metamorphic rocks, *J.Geophys. Res., 104*, 24,195-24,210.

Ghiorso, M.S. and R.O. Sack (1995), Chemical mass transfer in magmatic processes, IV. A revised and internally consistent thermodynamic model for the interpolation and extrapolation of liquid-solid equilibria in magmatic systems at elevated temperatures and pressures, *Contr. Mineral. and Petrol.*, 119, 197-212.

Hamilton, V.E., P.R. Christensen, and H.Y. McSween (1997), Determination of martian meteorite lithologies and mineralogies using vibrational spectroscopy, *J. Geophys. Res., 102*, 25,593-25,603.

Hamilton, V.E. (1999), The effect of particle size on rock spectra in the thermal infrared: Implications for TES data analysis, Lunar Plan. Sci. [CD-ROM], XXX, Abstract.

Hamilton, V.E and P.R. Christensen (2000), Determining the modal mineralogy of mafic and ultramafic rocks using thermal emission spectroscopy, *J. Geophys. Res., 105*, 9717-9733.

Hamilton, V.E., M.B. Wyatt, H.Y. McSween, and P.R. Christensen (2001), Analysis of terrestrial and martian volcanic compositions using thermal emission spectroscopy: 2. Application of martian surface spectra from the Mars Global Surveyor Thermal Emission Spectrometer, *J. Geophys. Res.*, *106,* 14,733-14,746.

Hamilton, V.E. and P.R. Christensen (2005), Evidence for extensive, olivine-rich bedrock on Mars, *Geology, 33*, 433-436.

Hoefen, T.M., R.N. Clark, J.L. Bandfield, M.D. Smith, J.C. Pearl, and P.R. Christensen (2003), Discovery of olivine in the Nili Fossae region of Mars, *Science, 302*, 627-630.

Irvine. T.N. and W.R. Baragar (1971), A guide to the chemical classification of common volcanic rocks, *Can. J. Earth Sci., 8*, 523-548.

Johnson, M.C., M.J. Rutherford, and P.C. Hess (1991) Chassigny petrogenesis: Melt compositions, intensive parameters, and water contents of martian (?) magmas. Geochimica et Cosmochimica Acta, *55*, 349-366.

Johnson, P.E., M.O. Smith, S. Taylor-George, and J.B. Adams (1983), A semiempirical method for the analysis of the reflectance spectra of binary mixtures, *J. Geophys. Res., 8*, 3557-3561.

Johnson, P.E., M.O. Smith, and J.B. Adams (1992), Simple algorithms for remote determination of mineral abundances and particle sizes from reflectance spectra, *J. Geophys. Res., 7,* 2649-2657.

Le Bas, M.J., R.W. Le Maitre, A. Streckeisen, and B.A. Zanettin (1986), Chemical classification of volcanic rocks based on the total alkali-silica diagram: *J. Petrology*, *27*, 745-750.

LeMaitre, R.W. (1989), Some problems of the projection of chemical data into mineralogical classifications, *Contrib. Mineral. Petrol., 56*, 181-189.

MacDonald, G.A. and T. Katsura (1964) Chemical composition of Hawaiian lavas, J. *Petrology, 5,* 82-133.

MacDonald, G.A. and D.K. Bailey (1973) The chemistry of peralkaline oversaturated obsidians, *Prof. Pap. U.S. Geol. Surv., 440N-1.*

Milam, K.A., H.Y. McSween, V.E. Hamilton, J.E. Moersch, and P.R. Christensen (2004), Accuracy of plagioclase compositions for laboratory and Mars spacecraft thermal emission spectra, *J. Geophys. Res., 109*, doi:10.1029.2003JE002097.

Moersch, J.E. and P.R. Christensen (1995), Thermal emission from particulate surfaces: A comparison of scattering models with measured spectra, *J. Geophys. Res., 100,* 7465-7477.

Nekvasil, H., J. Filiberto, M. Whitaker, and D.H. Lindsey (2003), Magams parental to the Chassigny meteorite: New considerations, Abstract, 6th International Mars Conference.

Norrish, K. and J.T. Hutton (1969), An accurate X-ray spectrographic method for the analysis of a wide range of geologic samples, *Geochim. Cosmochim. Acta, 33*, 431-453.

Ramsey, M. and P.R. Christensen (1998), Mineral abundance determination: Quantitative deconvolution of thermal emission spectra, *J. Geophys. Res., 103*, 577-596.

Ruff, S.W., P.R. Christensen, P. Barbera, and D. Anderson (1997), Quantitative thermal emission spectroscopy of minerals: A laboratory technique for measurement and calibration: *J. Geophys. Res.*, *102*, 14,899-14,913.

Ruff, S.W. (1998), Quantitative thermal emission spectroscopy applied to granitoid petrology, Ph.D. dissertation, 234 pp., Ariz. State Univ., Tucson.

Salisbury, J.W. and A. Wald (1992), The role of volume scattering in reducing spectra contrast of restrahlen bands in spectra of powdered minerals, *Icarus, 96*, 121-128.

Smith, M.D., J.L. Bandfield, and P.R. Christensen (2000), Separation of atmospheric and surface spectral features in Mars Global Surveyor Thermal Emission Spectrometer (TES) spectra, J. Geophys. Res., 105, 9589-9607.

Stolz, A.J. (1985), The Role of Fractional Crystallization in the Evolution of the Nandewar Volcano, Northeastern New South Wales, Australia: *J. Petrology, 26*, 1002-1026.

Stolz, A.J. (1986), Mineralogy of the Nandewar Volcano, northeastern New South Wales, Australia: *Mineralogical Magazine, 50*, 241-255.

Strekheisen, A.L. (1976), To each plutonic rock its proper name, *Earth Sci. Rev., 12,* 1-34.

Taylor, L.A., A. Patchen, D.H.S. Taylor, J.G. Chambers, and D.S. McKay (1996), X-ray digital imaging and petrology of lunar mare soils: Data input for remote sensing calibrations, *Icarus, 124*, 500-512.

Thomson, J.L. and J.W. Salisbury (1993), The mid-infrared reflectance of mineral mixtures (7-14 μm), *Remote Sens. Environ., 45*, 1-13.

Walter, L.S. and J.W. Salisbury (1989), Spectral characterization of igneous rocks in the 8- to 12-μm region, *J. Geophys. Res., 94*, 9203-9213.

Wyatt, M.B., V.E. Hamilton, H.Y. McSween, P.R. Christensen, and L. Taylor (2001), Analysis of terrestrial and martian volcanic compositions using thermal emission

spectroscopy: 1. Determination of mineralogy, chemistry, and classification strategies, *J. Geophys. Res.*, *106*, 14711-14732.

Wyatt, M.B. and H.Y. McSween (2002), Spectral Evidence for weathered basalt as an alternative to andesite in the northern lowlands of Mars, *Nature*, *417*, 263-266.

Wyatt, M.B., H.Y. McSween, K.L. Tanaka, and J.W. Head (2004) Global geologic context for rock types and surface alteration on Mars, *Geology, 32*, 645-648.

APPENDIX

Table 1. Major and Minor Element Analyses of Nandewar Alkalic Rocks[a]

Sample	Ref.[b]	SiO_2	TiO_2	Al_2O_3	FeO	Fe_2O_3	MnO	MgO	CaO	Na_2O	K_2O	P_2O_5	H_2O	Total
Basalts														
49000	1	46.99	2.65	14.55	8.90	1.77	0.13	8.18	8.97	2.80	1.43	0.47	3.13	99.97
49005	1	47.06	2.79	14.88	8.58	3.17	0.15	5.76	7.51	3.54	2.13	1.60	2.71	99.88
Trachyandesites														
49012	1	50.99	2.30	15.92	6.56	4.04	0.14	3.27	6.54	4.47	2.49	1.24	2.00	99.96
49074	1	57.46	1.00	17.46	2.85	3.49	0.09	1.30	3.14	5.16	4.75	0.60	2.31	99.61
Trachytes														
15800	2	60.14	0.77	17.07	2.98	2.63	0.16	0.78	2.76	4.87	5.26	0.31	0.05	97.78
49083	1	59.89	0.93	16.44	2.81	3.81	0.12	0.66	2.38	5.39	5.46	0.39	1.79	100.07
49098	1	62.73	0.54	15.18	3.82	3.02	0.20	0.16	1.60	6.60	5.16	0.06	0.49	99.56
15802	2	65.59	0.41	16.45	1.62	2.11	0.08	0.14	0.36	7.02	5.57	0.07	0.09	99.51
Rhyolites														
15806	2	72.70	0.13	13.20	0.54	2.60	0.05	0.08	0.09	6.01	4.50	0.04	0.19	100.13
15807	2	72.99	0.26	13.44	0.28	1.51	0.03	0.06	0.17	5.46	5.33	0.07	0.11	99.71
49130	1	74.55	0.27	13.82	0.20	0.87	0.01	0.01	0.12	4.82	5.10	0.02	0.16	99.95

[a]Values are in weight percent oxides.

[b]1 *Stolz* (1985); 2 *Abbott* (1969)

Table 2. Classification of Nandewar Alkalic Rock Samples

Sample	Ref.[a]	Classification[b]	Chemical Classifcation[c]
49000	1	Hawaiite	Basalt
49005	1	Trachyandesite	Trachybasalt
49012	1	Trachyandesite	Basaltic Trachyandesite
49074	1	Tristanite	Trachyandesite
15800	2	Mafic Trachyte	Trachyte
49083	1	Mafic Trachyte	Trachyte
49098	1	Peralkaline Trachyte	Trachyte
15802	2	Peralkaline Trachyte	Trachyte
15806	2	Peralkaline Rhyolite	Rhyolite
15807	2	Peralklaine Rhyolite	Rhyolite
49130	1	Peraluminous Rhyolite	Rhyolite

[a]1 *Stolz* (1985); 2 *Abbott* (1969)

[b]Classification as determined by *Abbott* (1969) or *Stolz* (1985)

[c]Chemical classification based on *Le Bas* (1986)

Table 3. Concentration Criteria Used to Classify Minerals and Glasses

Phase	Defining Criteria[a]
Plagioclase	43-70% Si, 17-43% Al, 9-27% Ca, <5% K
Alkali feldspar	55-75% Si, 10-30% Al, <6% Ca, 8-20% K
Quartz	88-100% Si
Silica-K_2O Glass	54-76% Si, 15-30% Al, 1.5-8% K
Silica glass	75-85% Si, 5-15% Al
Amphibole	45-70% Si, <12% Ca, 15-40% Fe
Ca-Pyroxene	41-60% Si, 22-61% Ca, 2-13% Fe, <9% Al
Na-pyroxene	60-76% Si, 19-30% Fe, <5% Na
Illmenite	30-60% Fe, 45-70% Ti
Magnetite	5-45% Ti, >54% Fe
Apatite	45-65% Ca, 15-44% P, <15% Si
Olivine	33-55% Si, 11-41% Mg, 0-4% Ca
Siderite	1-30% Ca, 60-90% Fe, 0-4% Ti

[a]Criteria used to classify minerals and glasses are in terms of percentage of spectrum. Values are similar to oxide weight %.

Table 4. Major Element Analysis of Minerals Added to Spectral Library[a]

Sample	SiO_2	Al_2O_3	FeO	MgO	CaO	Na_2O	MnO	K_2O	TiO_2	P_2O_5	Total
Aegirine	50.94	0.78	30.56	0.17	2.61	12.48	0.71	0.19	1.65	0.02	100.11
Aenigmatite	44.46	2.45	38.14	0.42	1.73	8.83	0.67	0.85	2.22	0.01	99.78
Arfvedsonite	47.08	2.54	38.62	0.13	1.60	7.85	0.56	1.87	0.52	0.01	100.78
Omphacite	54.61	2.20	3.54	22.06	9.99	4.95	0.19	1.55	0.53	0.02	99.64
Richterite	42.50	2.45	36.67	0.91	1.92	8.83	0.65	0.88	2.12	0.02	96.95
Sanidine	64.79	18.63	0.51	0.15	0.74	2.79	0.01	11.01	0.08	0.03	98.74

[a]Values are in weight percent oxides

Table 5. End-member Mineral Compositions Used in Deconvolutions[a]

	SiO_2	Al_2O_3	FeO	MgO	CaO	Na_2O	MnO	K_2O	TiO_2	Cr_2O_3	P_2O_5	Total
Feldspars												
Albite WAR-0244	69.16	18.18	0.24	0.01	0.38	10.20	0.01	0.66	0.01	0.02	0.38	99.25
Andesine BUR-240	53.85	27.09	0.53	0.07	9.51	5.55	0.01	0.34	0.12	0.02	0.1	97.19
Anorthoclase WAR-0579	62.86	19.90	0.30	1.01	2.64	5.77	0.04	4.32	0.15	0.20	0.06	97.25
Labradorite WAR-4524	52.62	27.74	2.50	0.14	10.90	5.01	0.02	0.42	0.11	0.00	0.04	99.50
Microcline BUR-3460	63.45	19.12	0.13	0.01	0.16	2.77	0.01	12.03	0.01	0.01	0.56	98.26
Microcline WAR-5802	67.20	18.57	0.14	0.24	0.45	5.14	0.01	7.18	0.01	0.12	0.02	99.08
Oligoclase WAR-0234	60.79	22.05	0.00	0.85	5.37	6.71	0.02	0.91	0.02	0.10	0.02	96.84
Oligoclase BUR-3680	63.48	22.74	0.03	0.44	4.94	7.76	0.13	0.63	0.01	0.16	0.02	100.34
Oligoclase BUR-5804	60.08	22.29	0.17	0.01	4.01	8.48	0.01	0.71	0.01	0.01	0.06	95.84
Sanidine NMNH-94412	64.79	18.63	0.51	0.15	0.74	2.79	0.01	11.01	0.08	0.00	0.03	98.74
Silica												
Quartz BUR-4120	100.00	0.00	0.00	0.00	0.00	0.00	0.00	0.00	0.00	0.00	0.00	100.00
Silica glass[b]	99.99	0.00	0.00	0.00	0.00	0.00	0.00	0.00	0.00	0.00	0.00	99.99
Silica-K_2O glass[b]	77.87	0.00	12.55	0.00	0.00	0.00	0.00	3.90	5.67	0.00	0.00	99.99
Pyroxenes												
Aegerine NMNH-95509	50.94	0.78	30.57	0.17	2.61	12.48	0.71	0.19	1.65	0.00	0.02	100.12
Aenigmatite NMNH-133756	44.46	2.45	38.14	0.42	1.73	8.83	0.67	0.85	2.22	0.00	0.01	99.78
Augite BUR-620	50.51	1.69	16.90	7.58	21.51	1.91	0.73	0.00	0.11	0.00	0.00	100.94
Augite HS-119.4B	52.87	0.92	10.46	11.91	24.08	0.65	0.29	0.00	0.02	0.00	0.00	101.20
Augite-5858	50.58	3.23	7.13	16.82	19.81	0.36	0.16	0.01	0.79	0.00	0.00	98.89
Bronzite NMNH-34669	57.03	0.39	6.36	35.46	0.11	0.01	0.15	0.00	0.00	0.00	0.00	99.51
Diopside NMNH-107497	54.99	0.31	0.85	18.17	25.40	0.10	0.02	0.00	0.01	0.00	0.00	99.85
Diopside WAR-6474	50.60	2.35	13.28	9.96	21.13	2.00	0.30	0.00	0.18	0.00	0.00	99.80
Diopside BUR-1820	54.30	0.31	2.67	16.68	25.29	0.23	0.13	0.00	0.05	0.00	0.00	99.66
Diopside HS-317.4B	51.87	0.91	3.82	16.37	21.75	1.10	0.08	0.00	0.00	0.29	0.00	96.19

Table 5. continued

	SiO_2	Al_2O_3	FeO	MgO	CaO	Na_2O	MnO	K_2O	TiO_2	Cr_2O_3	P_2O_5	Total
Enstatite NMNH-120414-1	53.94	1.28	15.28	27.42	0.88	0.00	0.30	0.00	0.04	0.00	0.00	99.14
Enstatite HS-9.4B	57.87	0.99	6.94	34.86	0.67	0.00	0.17	0.00	0.02	0.00	0.00	101.52
Enstatite NMNH-119793	55.66	2.27	8.08	32.29	1.03	0.02	0.17	0.00	0.11	0.00	0.00	99.63
Hendenbergite DSM-HED01	49.96	0.06	14.14	4.32	22.80	0.11	7.99	0.00	0.10	0.00	0.00	99.48
Hypersthene NMNH-C2368	51.88	4.24	15.09	25.34	2.05	0.03	0.25	0.01	0.32	0.00	0.00	99.21
Hypersthene HS-205.4B	54.43	0.42	2.22	16.22	25.77	0.15	0.06	0.00	0.00	0.00	0.00	99.27
Jadeite WAR-9909	58.84	20.72	3.49	1.66	2.42	14.26	0.04	0.00	0.36	0.00	0.00	101.79
Omphacite NMNH-R3020	54.61	2.20	3.53	22.06	9.99	4.95	0.19	1.55	0.53	0.00	0.02	99.63
Olivines												
Forsterite AZ-01	38.47	0.09	9.57	48.88	0.14	0.03	0.13	0.01	0.01	0.08	0.01	97.42
Forsterite BUR-3720A	41.95	0.49	8.49	49.33	0.38	0.02	0.13	0.12	0.01	0.57	0.01	101.50
Amphiboles												
Arfvedsonite NMNH-133747	47.08	2.54	38.62	0.13	1.60	7.85	0.56	1.87	0.52	0.00	0.01	100.78
Hornblende HS-177.4B	42.93	2.27	11.38	15.45	0.11	11.21	12.05	2.12	1.53	0.11	0.12	99.28
Richterite NMNH-150800	42.50	2.45	36.67	0.91	1.92	8.83	0.65	0.88	2.12	0.00	0.02	96.95
Jade (Nephrite) WAR-0979	56.37	0.73	4.06	21.38	12.39	1.06	0.11	0.28	0.01	0.12	0.00	96.51
Hornblende WAR-0404	42.69	0.90	14.56	12.80	0.10	13.46	9.83	2.75	0.94	0.07	0.10	98.20
Non-silicates[c]												
Apatite P1 perp to a-axis												
Apatite P1 perp to c-axis												
Siderite C5	0.00	0.00	0.24	47.00	0.31	0.00	0.00	0.00	0.00	0.00	0.00	47.55

[a]Values are in weight percent oxides

[b]Synthetic samples from Wyatt et al., 2001

[c]Chemistry not available

Table 6. Electron Microprobe Measured Mineralogy

Sample	Feldspar		K_2O	SiO_2	Quartz	Pyroxene			Amphibole	Olivine	Apatite	Siderite	Fe-Oxides
	alkali	plag	glass	glass		cpx	opx	Na					
Basalts													
49000	6	36	25			16			<1	12	1		4
49005	18	23	34			8			1	9	2		4
Trachyandesites													
49012	18	10	58			7			<1	2	1		4
49074	53	14	19			8			7			3	2
Trachytes													
15800	66	6	17			2			7				2
49083	60	2				10			<1				
49098	73	6	8	2	4				2				5
15802	77	5	9	2	3			2	2				
Rhyolites													
15806	38	12	19	5	2				4				
15807	67		5	7	20				1				
49130	71		6		24								

Blank spaces represent phases not measured in a given sample.

Table 7. Deconvolved Bulk Mineralogy at 2 cm^{-1} Spectral Sampling

Sample	Feldspar		SiO_2	Quartz	Pyroxene			Amphibole	Olivine	Apatite	Siderite
	alkali	plag	Glass		cpx	opx	Na-rich				
Basalts											
49000	8	53			23		8	<1	4	2	3
49005	18	41	<1		4	1	22	1	4	4	6
Trachyandesites											
49012	18	46			6	16	4	3		1	4
49074	32	50			13	1	3				
Trachytes											
15800	43	43				11					3
49083	58	33		<1		4			3		3
49098	67					31					
15802	88							6	2	1	4
Rhyolites											
15806	72		7	15	<1		4	1		1	1
15807	83		5	10					1	<1	3
49130	73		4	17	1						

Blank spaces represent phases not measured in a given sample.

Table 8. Major Mineralogy and Bulk-Rock Chemistry Error Analysis

	Alkali Feldspar	Plagioclase	Silica Glass	Quartz	Clino-pyroxene	Ortho-pyroxene	Amphibole	Olivine	Apatite
Mean absolute difference	10.72	18.15	1.14	3.35	2.57	5.45	2.39	1.84	0.45
Standard deviation[a]	11.26	15.02	1.41	4.66	2.92	9.87	2.49	2.62	0.68
	SiO_2	Al_2O_3	FeO	MgO	CaO	Na_2O	MnO	K_2O	TiO_2
Mean absolute difference	3.76	1.45	3.26	2.44	1.73	1.42	0.17	1.42	0.96
Mean relative difference	0.06	0.09	0.77	1.20	0.82	0.28	0.91	0.21	1.36
Standard deviation[a]	2.38	0.99	2.25	2.80	1.24	1.29	0.23	0.55	0.92

[a]Standard deviation is of the absolute difference in mineral abundances as determined by the linear deconvolution and electron microprobe techniques

Table 9. Compositions of Glass Spectral End-members and Nandewar Glass[a]

	Silica-K_2O Glass[b]	Silica Glass[b]	Measured Glass
SiO_2	77.90	99.90	48.14
TiO_2	0.00	0.00	0.00
Al_2O_3	12.60	0.00	26.71
MgO	0.00	0.00	1.09
CaO	0.00	0.00	9.00
MnO	0.00	0.00	0.01
FeO	0.00	0.00	0.74
Na_2O	3.90	0.00	1.77
K_2O	5.67	0.00	1.70
Total	100.00	99.90	89.18

[a]Values are in weight percent oxides

[b]From Wyatt at al., 2001

Table 10. Summary of Volcanic Rock Classifications[a]

	Classification Schemes			
	Modeled Modal	Derived Mineral	Derived Bulk Rock Chemistry	
Sample	Mineralogy[b]	Chemistry[c]	Le Bas et al.[d]	Cox et al.[e]
Basalts				
49000	B	B	BA	BA
49005	B	TB	BTA/TA	TA
Trachyandesites				
49012	B	N/A	BTA (TA)	TA
49074	TA	N/A	TA	TA
Trachytes				
15800	TA	TB	T (TA)	TA
49083	TA	TB	T	T
49098	T	Tristanite	TA	TA
15802	T	T	T	T
Rhyolites				
15806	T	R	R	R
15807	T	R	R/T	R
49130	T	R	R (T)	R

[a]B, basalt; TB, trachybasalt; BTA, basaltic trachyandesite; TA, trachyandesite; T, trachyte; R, rhyolite; BA, basaltic andesite

[b]See Figure 10

[c]See Figure 11

[d]See Figure 12

[e]See Figure 13

Table 11. Deconvolved Bulk Mineralogy at 10 cm^{-1} Spectral Sampling

Sample	Feldspar		SiO_2 Glass	Quartz	Pyroxene			Amphibole	Olivine	Apatite	Siderite
	alkali	plag			cpx	opx	Na-rich				
Basalts											
49000	8	55			22		5		7		4
49005	9	46			11		16	1	8	5	5
Trachyandesites											
49012	23	38			4	2	13	12		2	6
49074	40	42			7	2		9			
Trachytes											
15800	51	30			3	3		9			5
49083	51	40		<1	1				6		2
49098	61				8	3		19			7
15802	86						2	5	3		4
Rhyolites											
15806	72		8	13		<1	3		<1	3	
15807	84		2	10						1	3
49130	71		6	17					1	3	3

Blank spaces represent phases that were not measured in a sample.

Table 12. Comparison of Uncertainties at 2 cm^{-1} and 10 cm^{-1} Spectral Sampling

	RMS Errors			Phase Standard Deviation (vol %)			Oxide Standard Deviation (wt %)		Mean Absolute Difference (wt %)	
Sample	2 cm^{-1}	10 cm^{-1}	Phase	2 cm^{-1}	10 cm^{-1}	Oxide	2 cm^{-1}	10 cm^{-1}	2 cm^{-1}	10 cm^{-1}
49000	0.327	0.294	Alkali Feldspar	11.26	9.13	SiO_2	2.38	2.11	3.76	3.62
49005	0.349	0.282	Plagioclase	15.02	12.85	TiO_2	0.92	0.90	0.96	0.92
49012	0.471	0.368	Silica glass	1.41	2.19	Al_2O_3	0.99	1.13	1.45	1.52
49074	0.444	0.409	Quartz	4.66	4.30	FeO	2.25	2.27	3.26	3.56
15800	0.359	0.282	Clinopyroxene	2.92	3.48	MnO	0.23	0.82	0.17	0.77
49083	0.343	0.297	Orthpyroxene	9.87	1.15	MgO	2.80	2.01	2.44	2.61
49098	0.613	0.339	Amphibole	2.59	5.40	CaO	1.24	0.75	1.73	1.26
15802	0.394	0.263	Olivine	2.62	2.26	Na_2O	1.29	1.47	1.42	1.45
15806	0.457	0.385	Apatite	0.68	1.24	K_2O	0.55	0.51	1.42	1.39
15807	0.519	0.493								
49130	0.428	0.386								

Table 13. Modal Mineralogies Derived From Martian Surface Spectra

	Surface Type 1: Basalt				Surface Type 2: Andesite		
Mineral Group	Christensen et al. [2000]	Bandfield et al. [2000]	Hamilton et al. [2001]	This work	Bandfield et al. [2000]	Hamilton et al. [2000]	This Work
Feldspar	45	50	55	35	35	49	30
Clinopyroxene	26	25	21	31	10		13
Glass			9	1	25	28	17
Sheet Silicate	15	15	5		15	8	
Orthopyroxene		5	8			8	2
Amphibole			2	5	6	4	9
Olivine	12			6	3	3	5
Na Pyroxene				16			17
Siderite				5			6

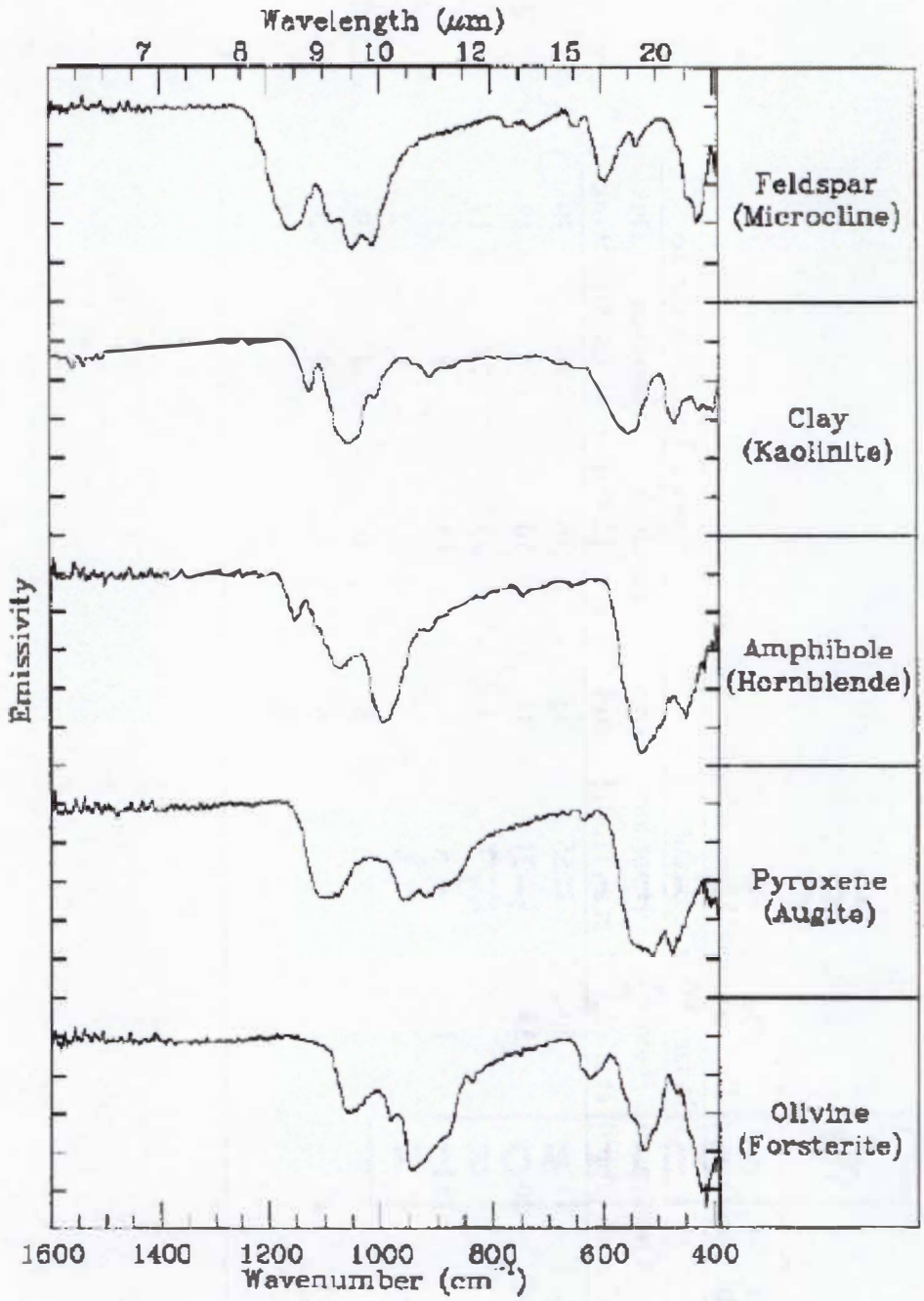


Figure 1. Thermal emissivity spectra of common rock-forming silicate minerals [*Christensen et al.*, 2000].

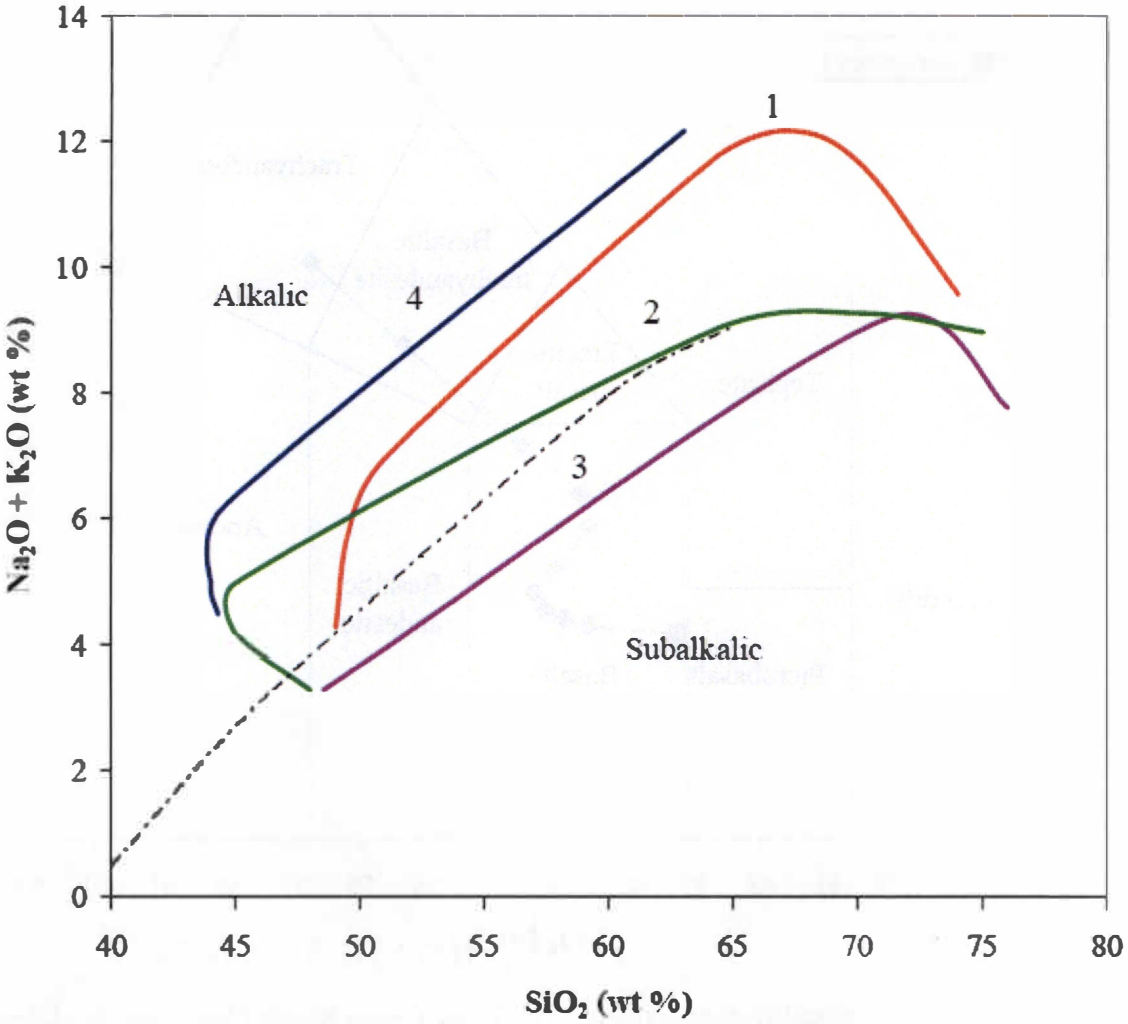


Figure 2. Four major trends of alkalic hot spot magmatism [from *Nekvasil et al.*, 2003]. Trend 1 shows the variation in lava compositions of sodic silica-saturated mildy alkalic suites; trend 2 shows the variation in lava compositions of potassic silica-saturated suites; trend 3 reflects the typical subalkalic tholeiitic provinces of ocean islands; and trend 4 includes silica-undersaturated alkali basalts.

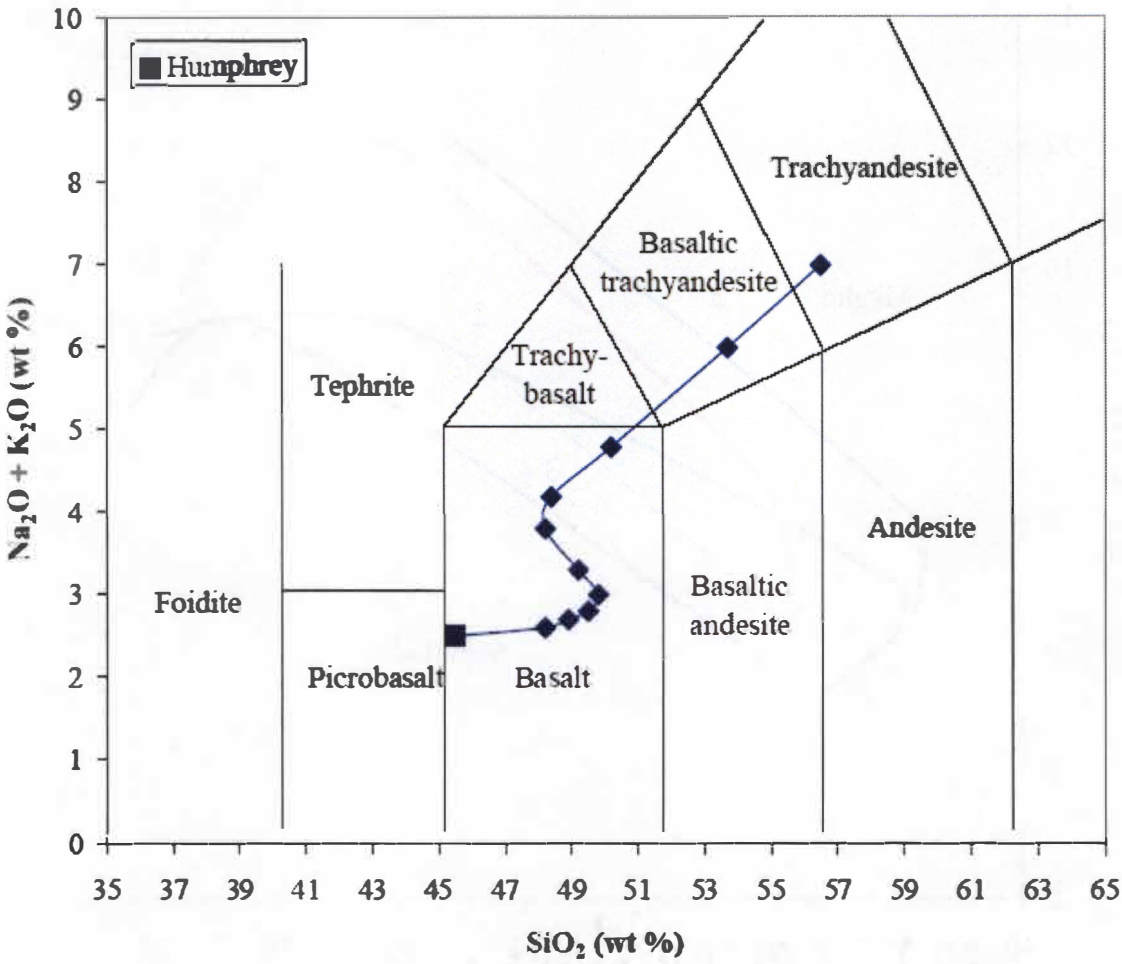


Figure 3. Fractional crystallization sequence of Gusev Crater basalt *Humphrey* modeled using MELTS program, developed by *Ghiorso and Sack* [1995]. The liquid line of descent of Humphrey follows an alkalic trajectory.

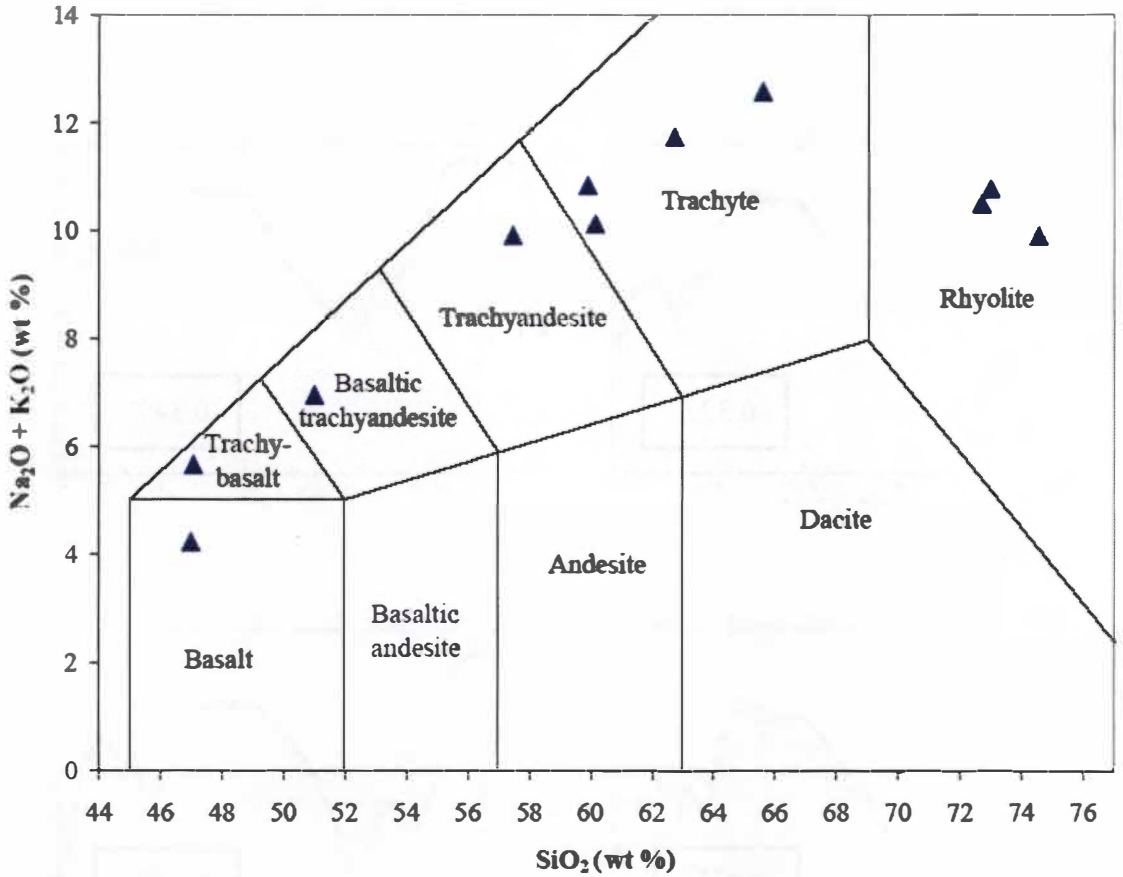


Figure 4. Chemical compositions of the Nandewar volcano alkalic rocks examined in this study.

a)

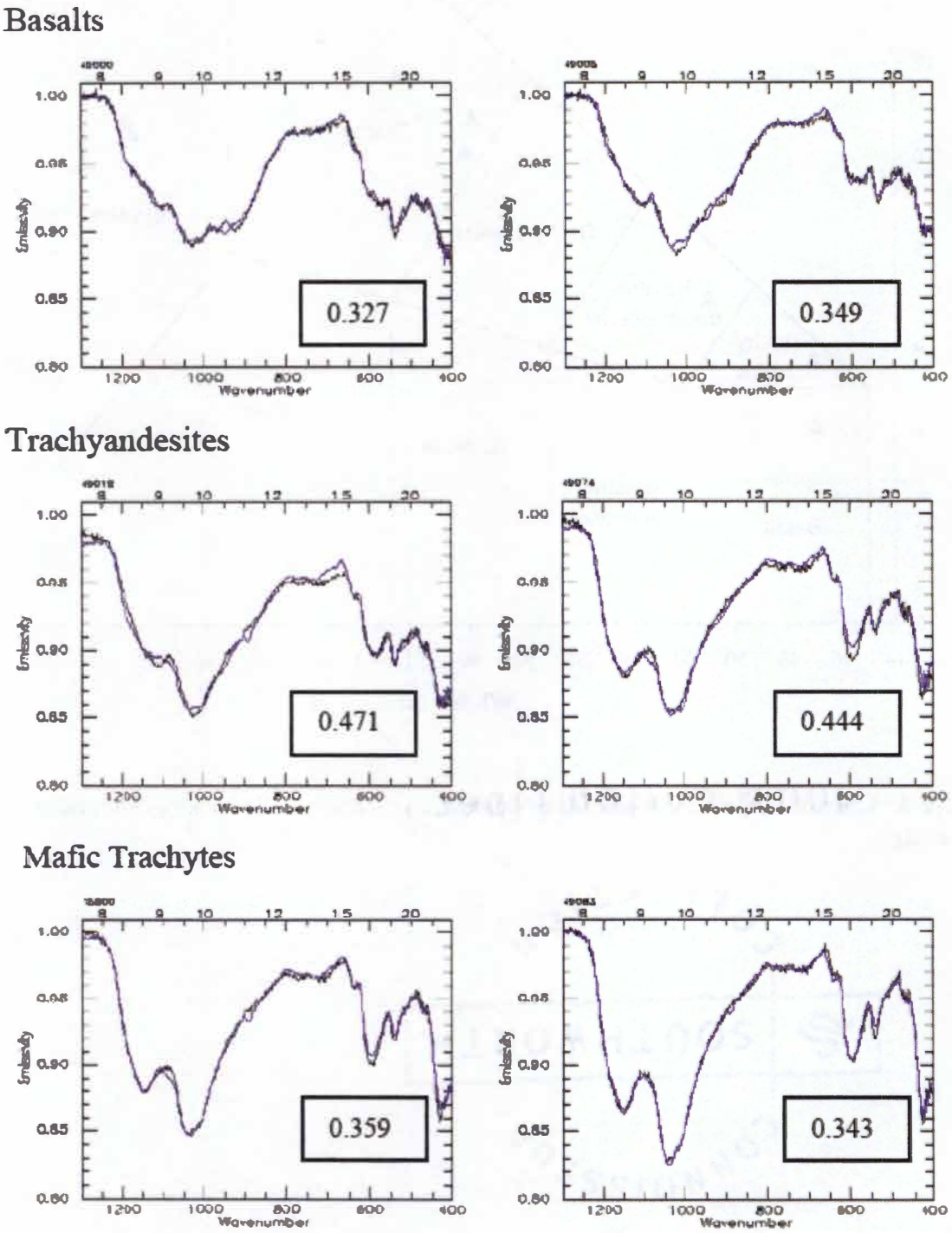
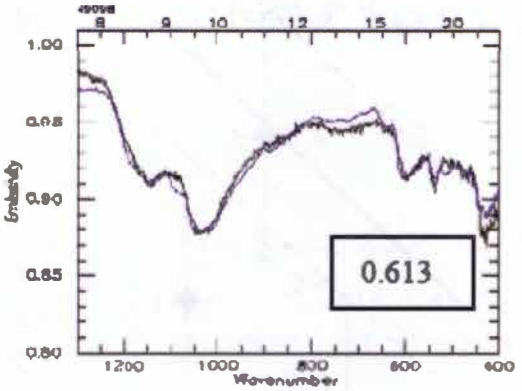
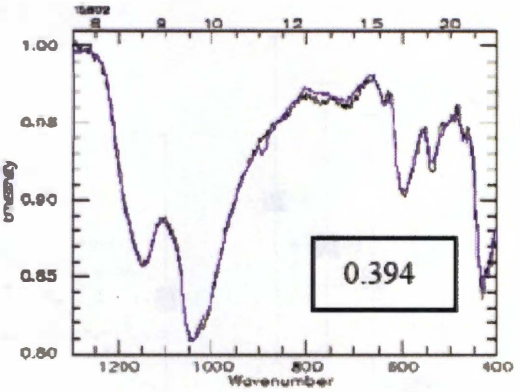


Figure 5. Measured (black) and modeled (purple) thermal emissivity spectra of (a) basalts, trachyandesites, and mafic trachytes. Enclosed boxes contain RMS errors for each sample.

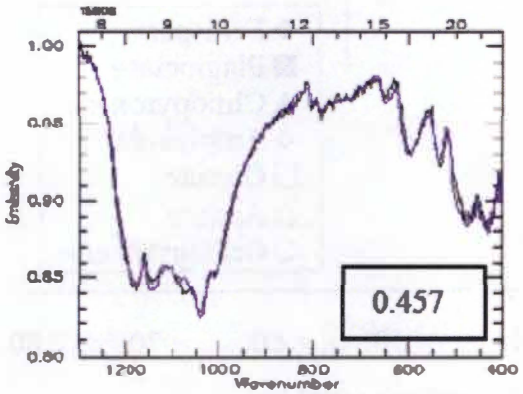
b)

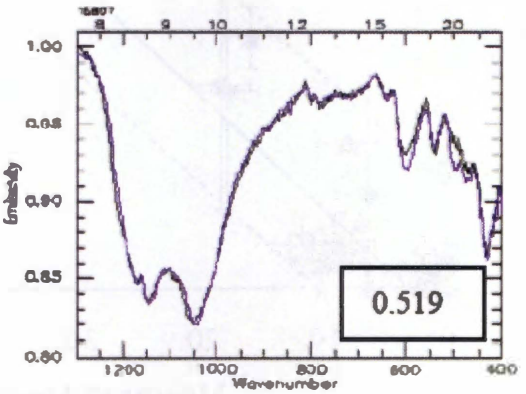
Peralkaline Trachytes





Rhyolites





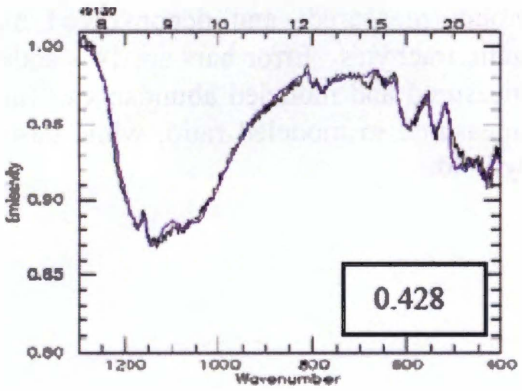


Figure 5 Continued. (b) peralkaline trachytes and rhyolites.

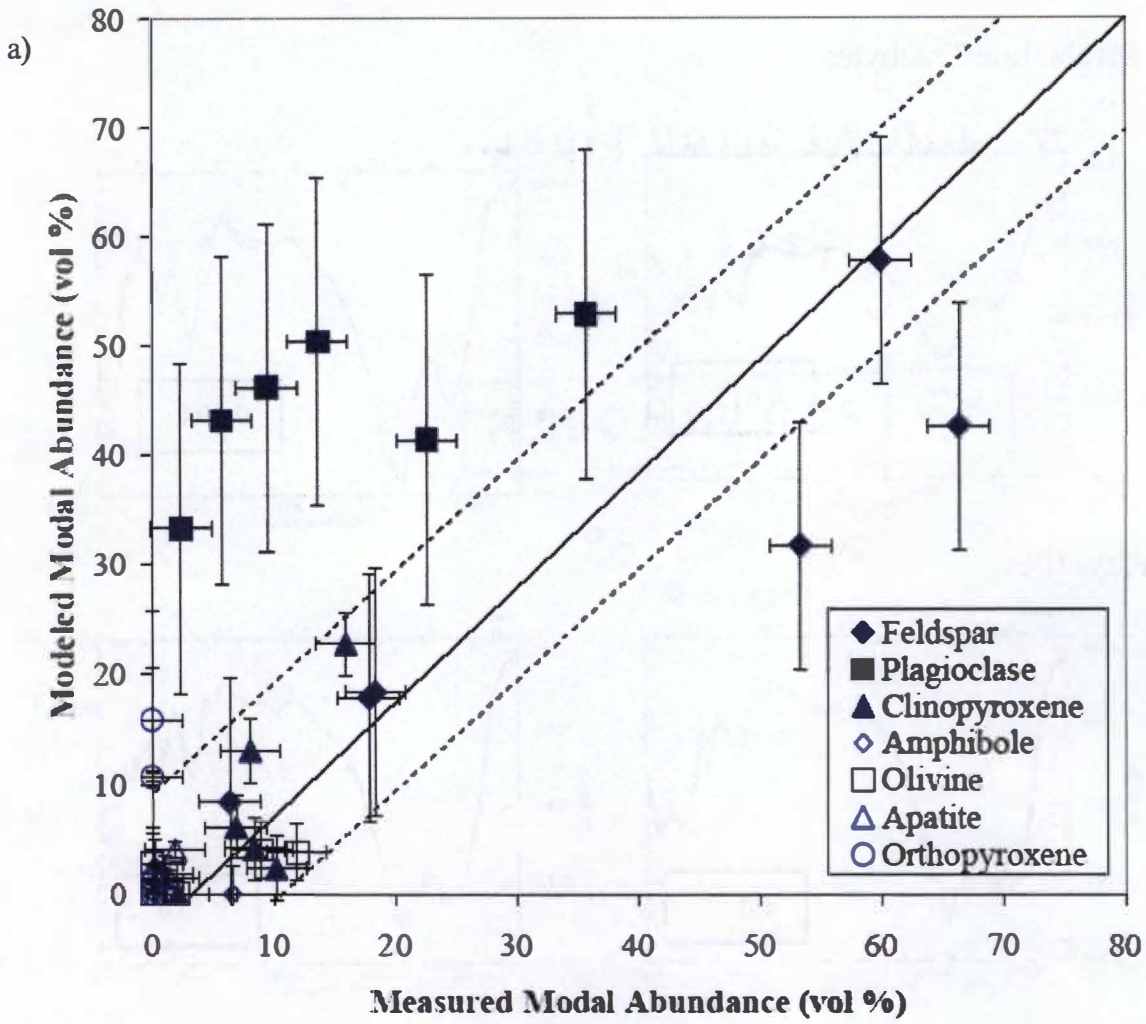


Figure 6. Comparison of electron microprobe (measured) and deconvolved bulk mineralogies for (a) basalts, trachyandesites, mafic trachytes. Error bars are 1σ standard deviation of the absolute difference between measured and modeled abundances (Table 8). The solid diagonal line represents a 1:1 measured to modeled ratio, while dashed diagonal lines establish the 10 vol % uncertainty field.

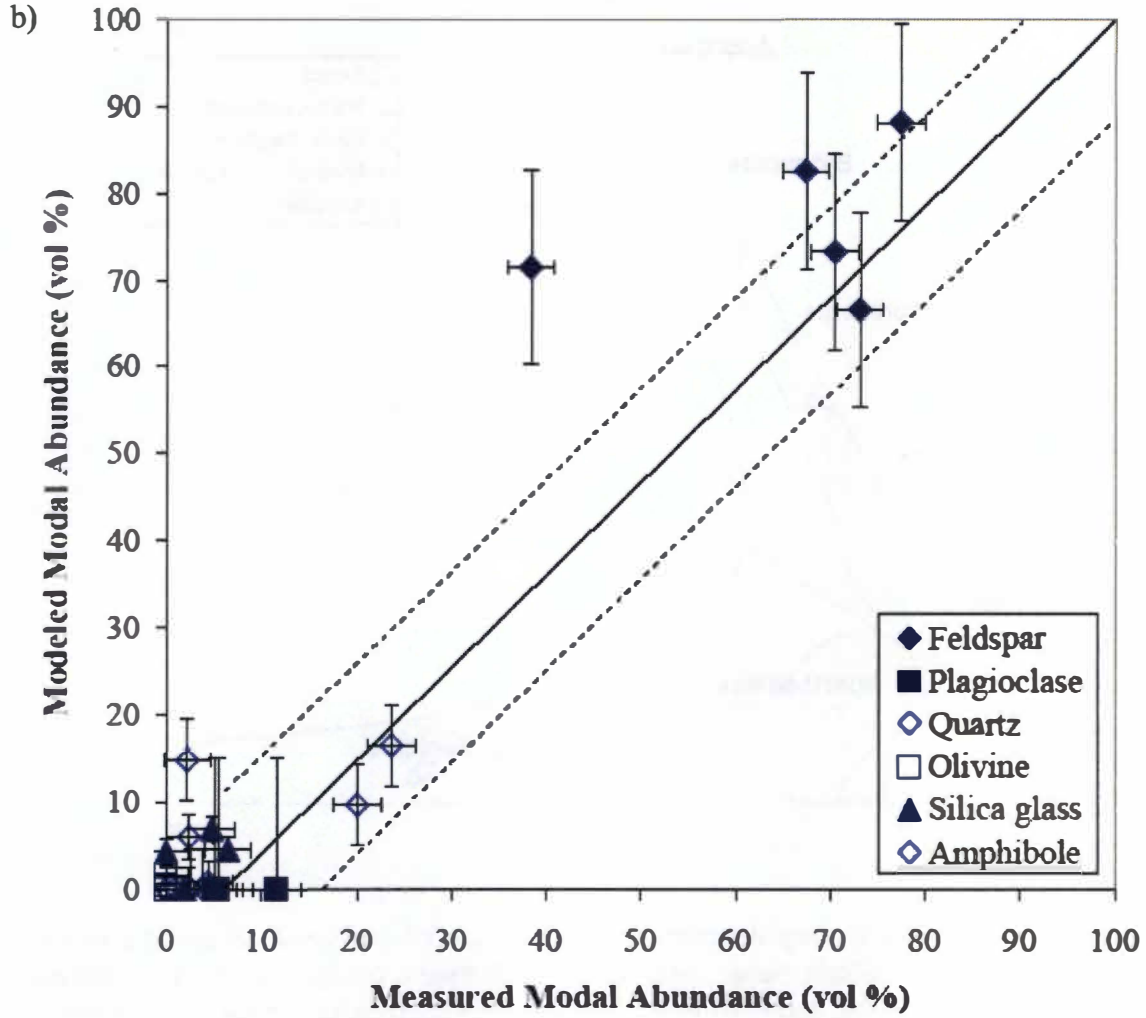


Figure 6 Continued. (b) peralkaline trachytes and rhyolites.

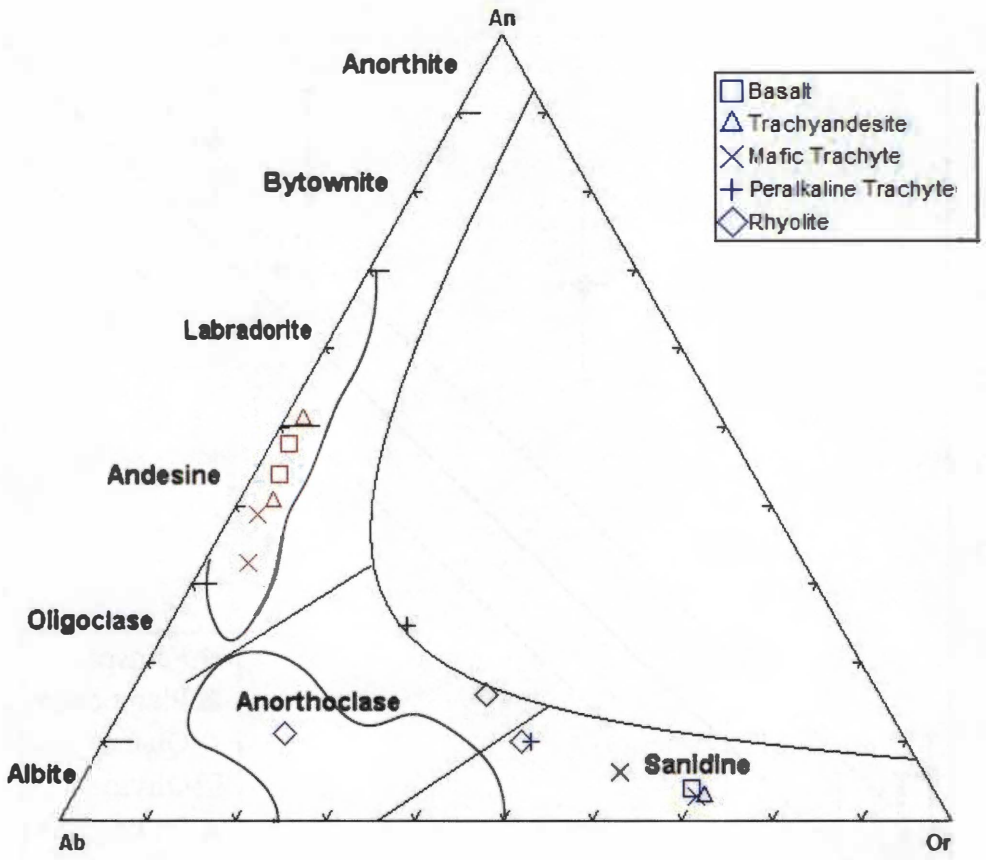


Figure 7. Or-Ab-An ternary diagram showing measured (enclosed areas) and model-derived (symbols) alkali and plagioclase feldspar compositions for basalts, trachyandesites, trachytes, and rhyolites. Symbols indicate measured rock chemistries.

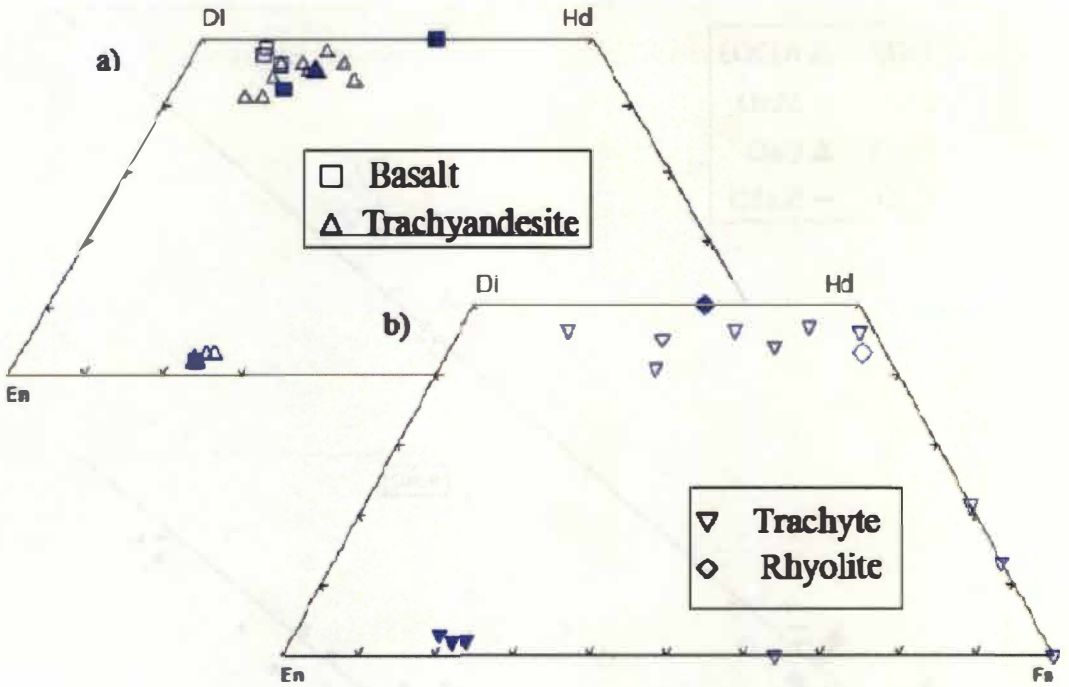


Figure 8. Deconvolved (closed symbols) and measured (open symbols) pyroxene compositions for (a) basalts and trachyandesites and (b) trachytes and rhyolites in the diopside (Di)- enstatite (En)- ferrosilite (Fs)- hedenbergite (Hd) system.

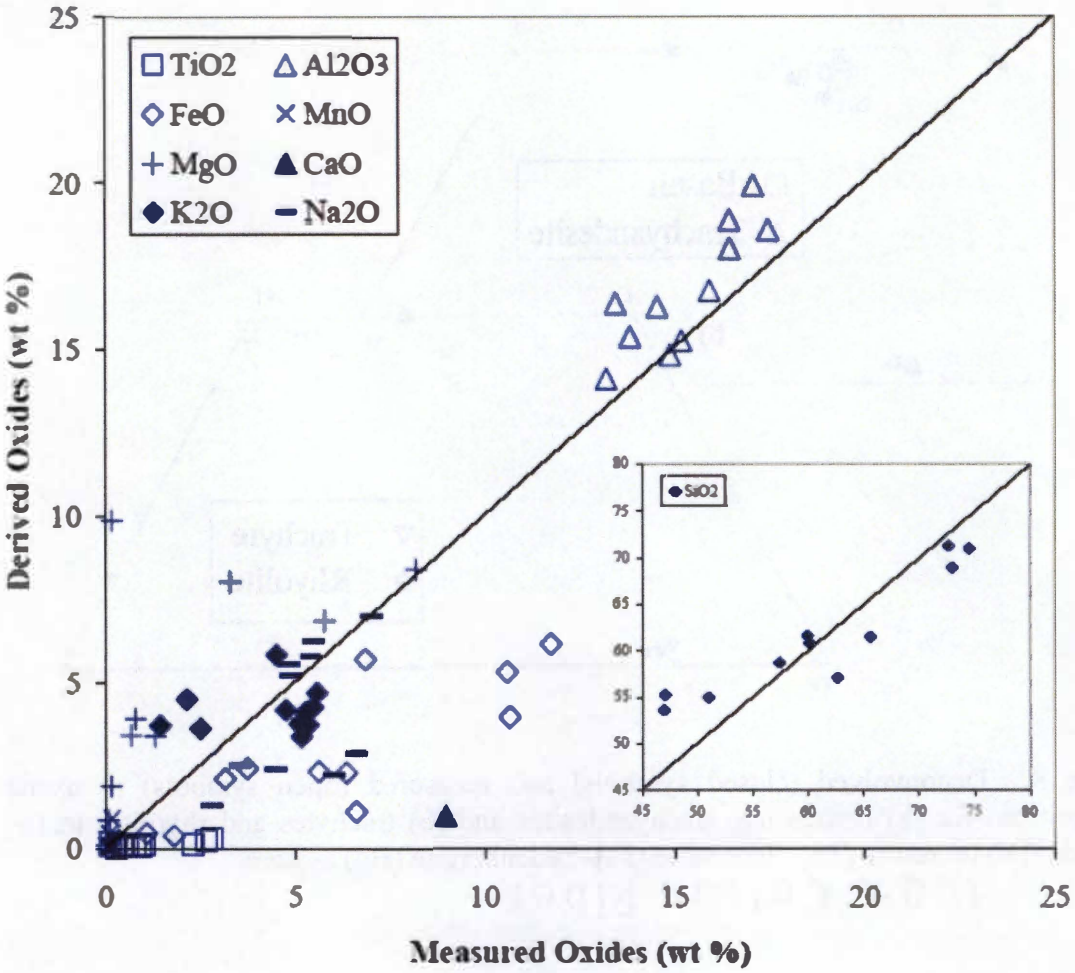


Figure 9. Measured versus derived oxide data (wt %) for basalts, trachyandesites, trachytes, and rhyolites. Silica abundances are shown in the smaller box. Uncertainties for each phase are listed in Table 8. The diagonal line is a 1:1 of measured to modeled oxides.

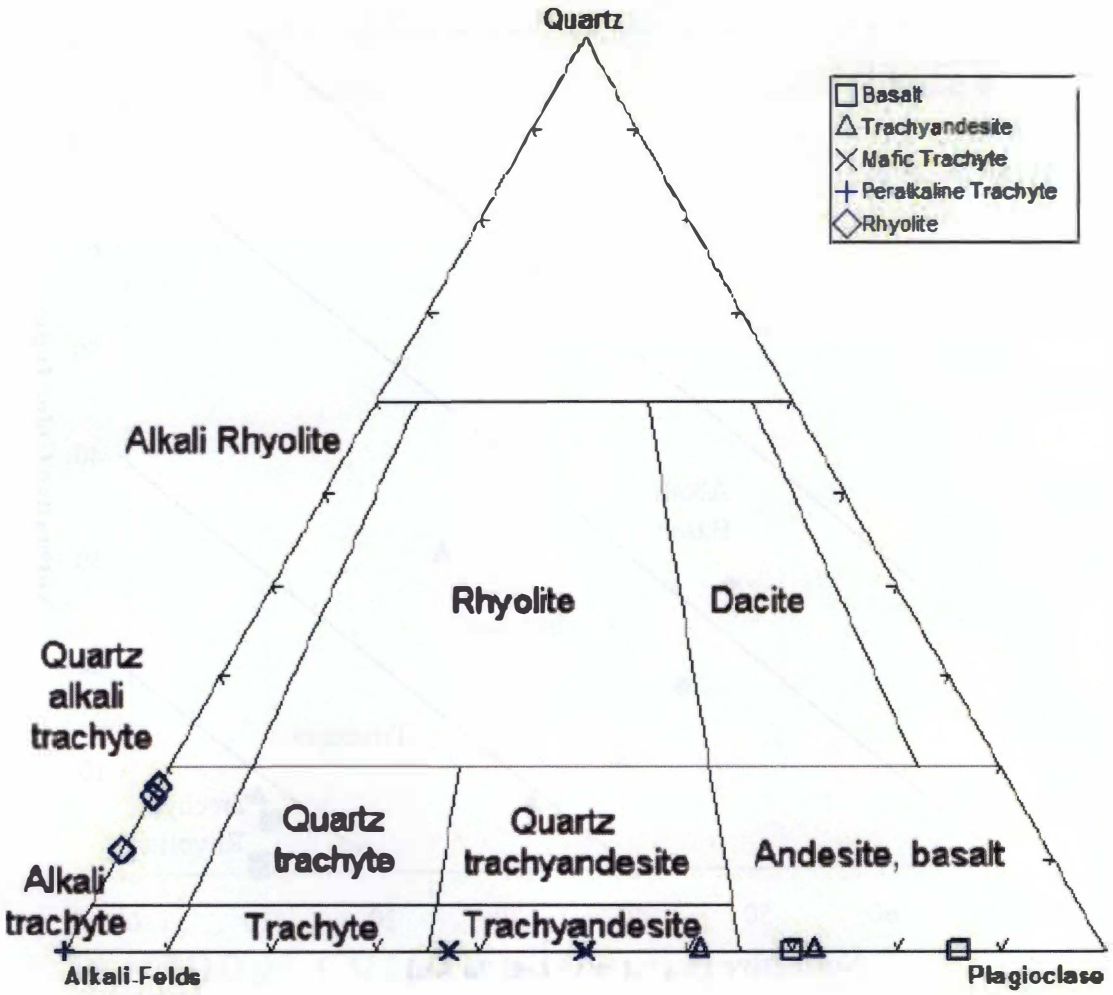


Figure 10. Model-derived modal mineralogies of basalt, trachyandesite, trachyte, and rhyolite samples. Symbols represent measured chemical compositions.

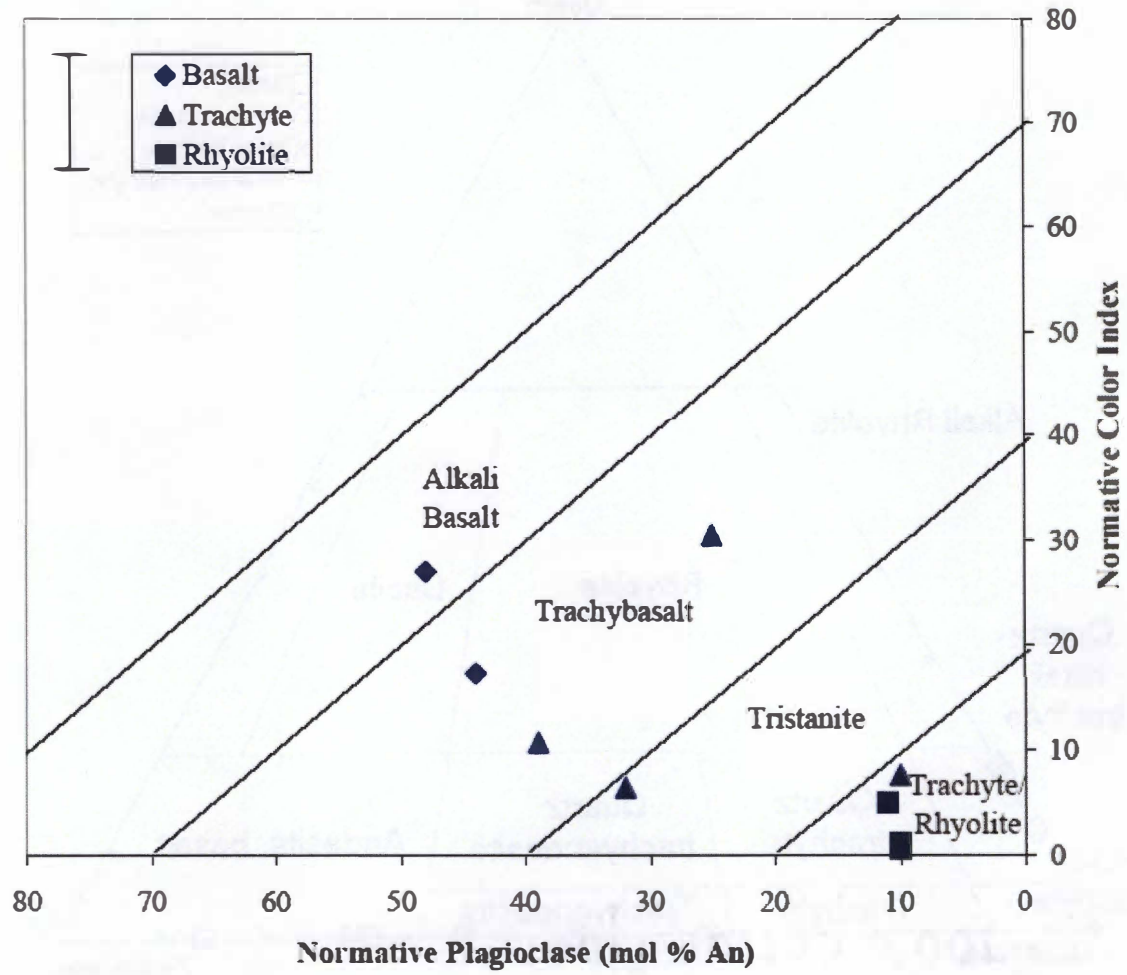


Figure 11. Normative plagioclase compositions (mol % An) versus normative color index (modal olivine + pyroxene + amphibole) for separating alkaline volcanic rocks [*Irvine and Baragar,* 1971]. Open symbols indicate measured rock compositions. Error bars for normative color index are the 1σ standard deviation for model-derived phases listed in Table 8. No standard deviation calculation is possible for normative plagioclase. (See text for discussion.)

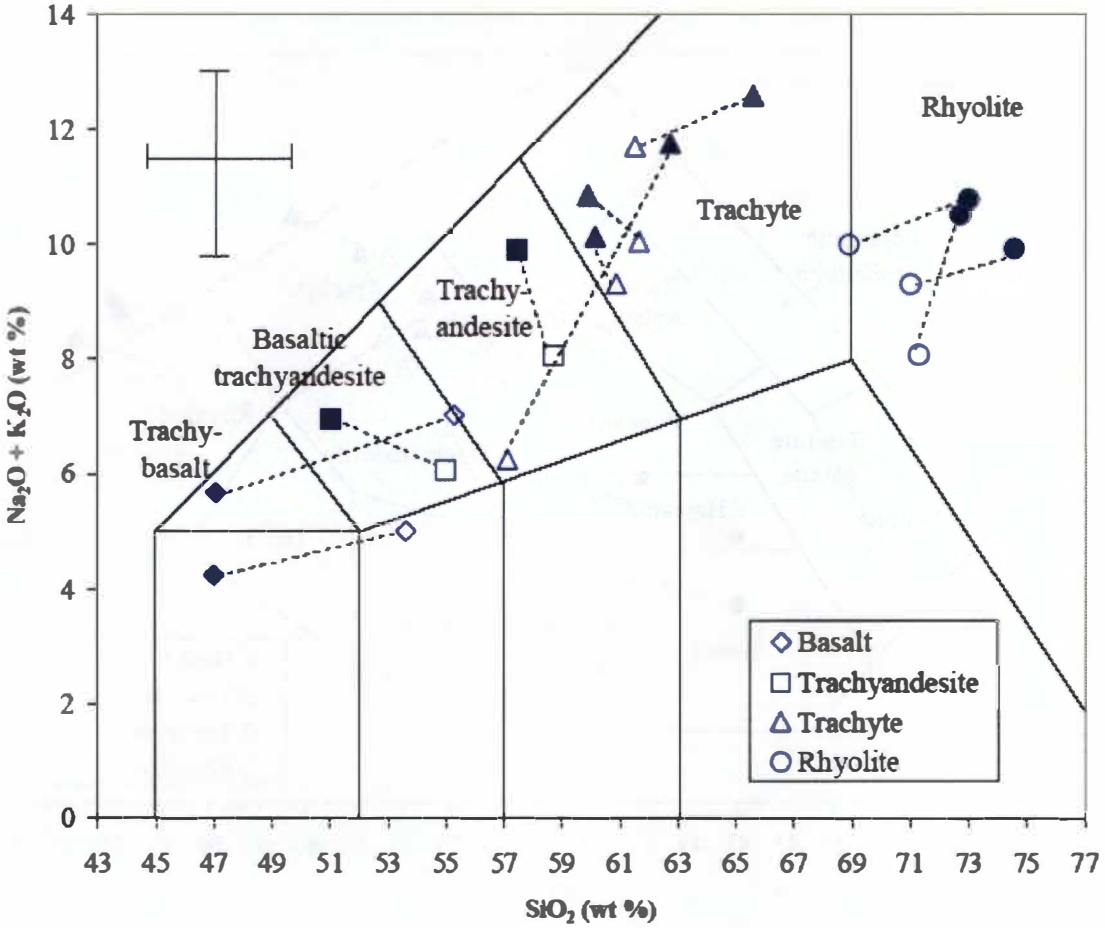


Figure 12. Measured (closed symbols) and modeled (open symbols) chemical compositions of basalts, trachyandesites, trachytes, and rhyolites. Error bars are 1σ standard deviations for silica and alkali oxides in Table 8.

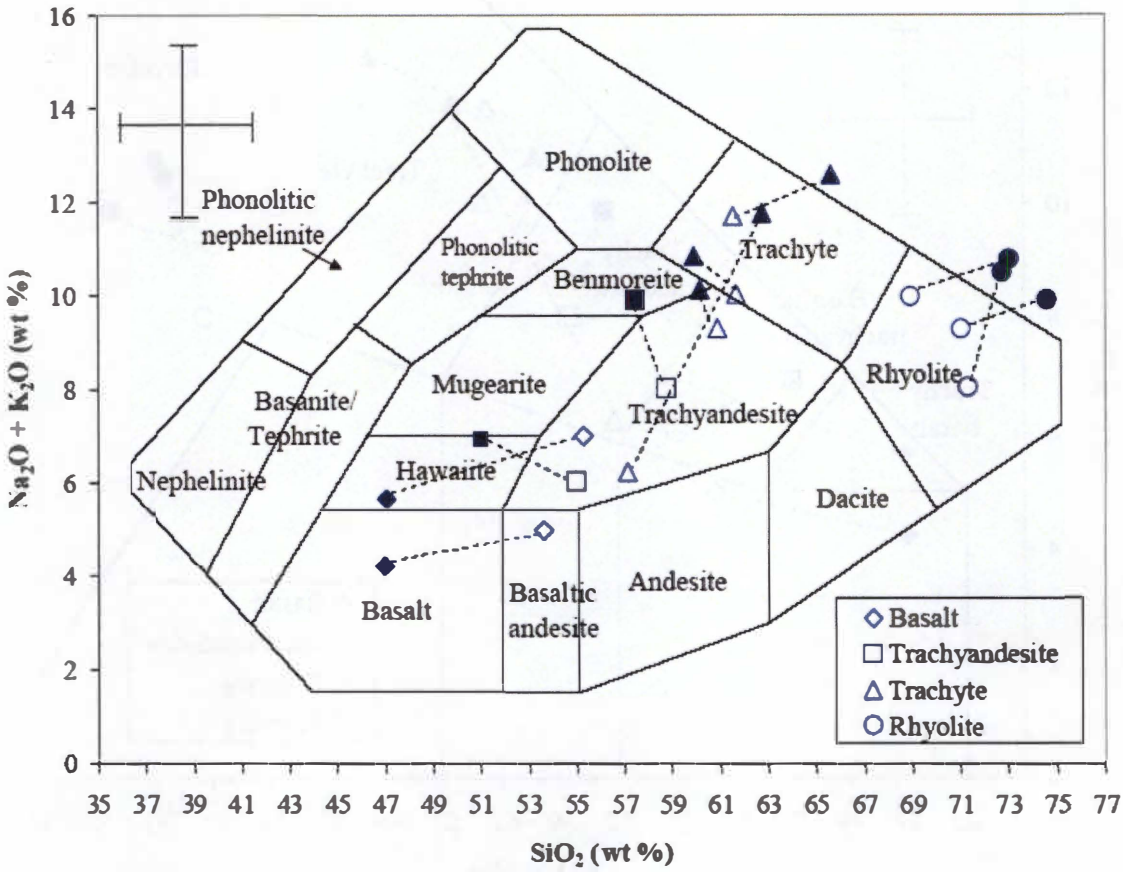
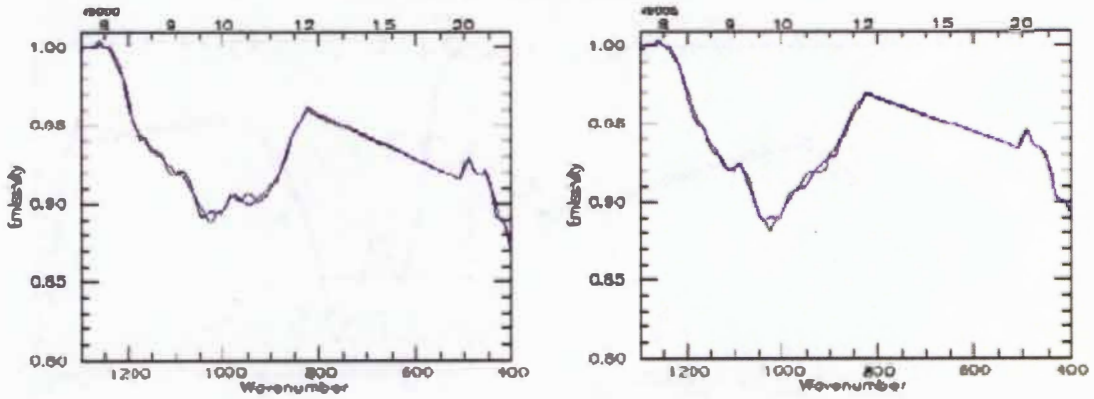


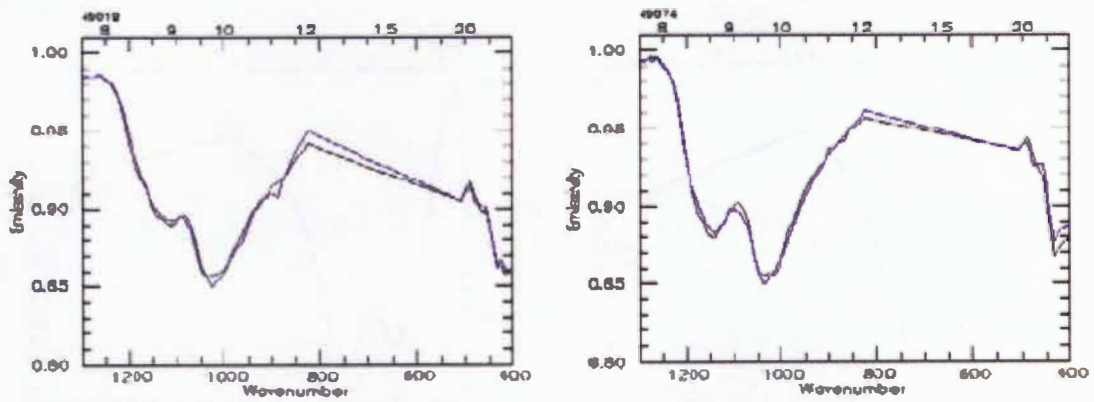
Figure 13. Derived (open symbols) and measured (closed symbols) silica and alkali oxides superimposed on the *Cox et al.* [1980] classification scheme for volcanic rocks. Symbols indicate measured compositions. Error bars are 1σ standard deviations for silica and alkali oxides in Table 8.

a)

Basalts



Trachyandesites



Mafic Trachytes

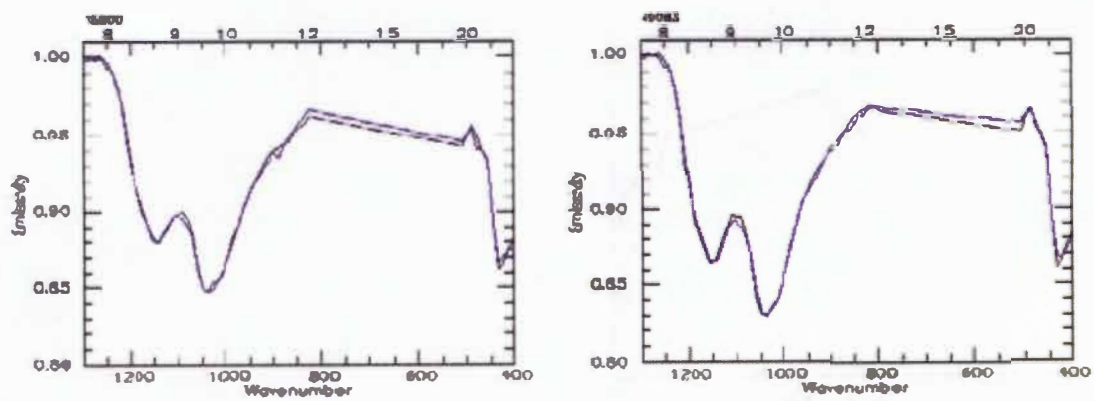
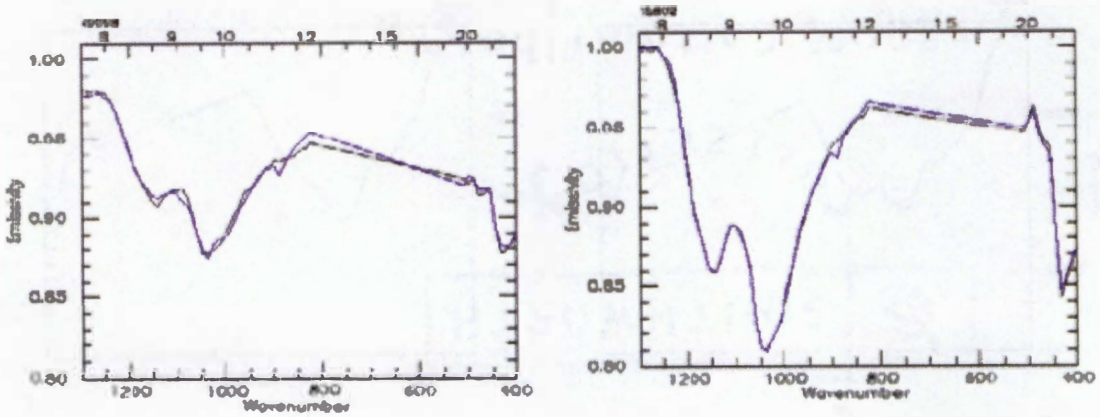


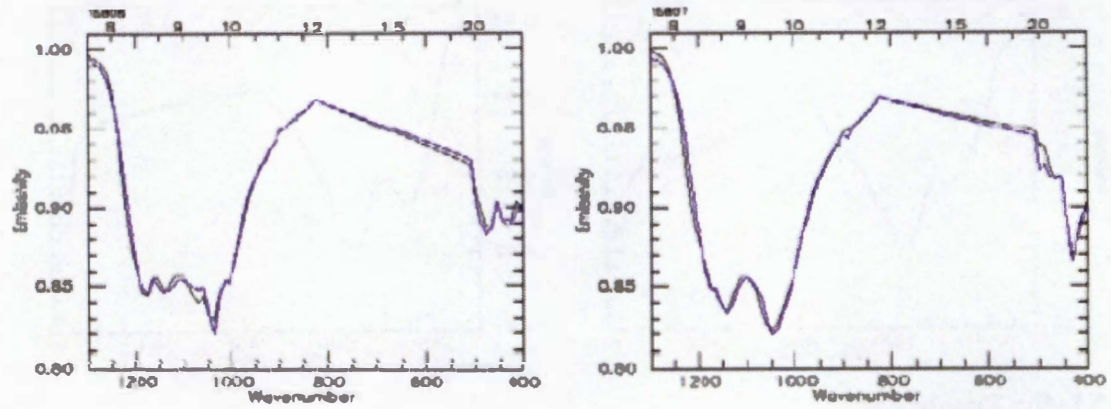
Figure 14. Measured (black) and modeled (purple) thermal emissivity spectra at 10 cm^{-1} resolution of (a) basalts, trachyandesites, and mafic trachytes. Spectra are shown at 10 cm^{-1} resolution. RMS errors are listed in Table 12.

b)

Peralkaline Trachytes



Rhyolites



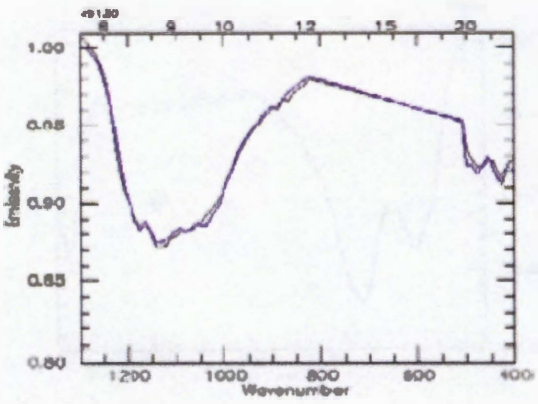


Figure 14 Continued. (b) peralkaline trachytes and rhyolites.

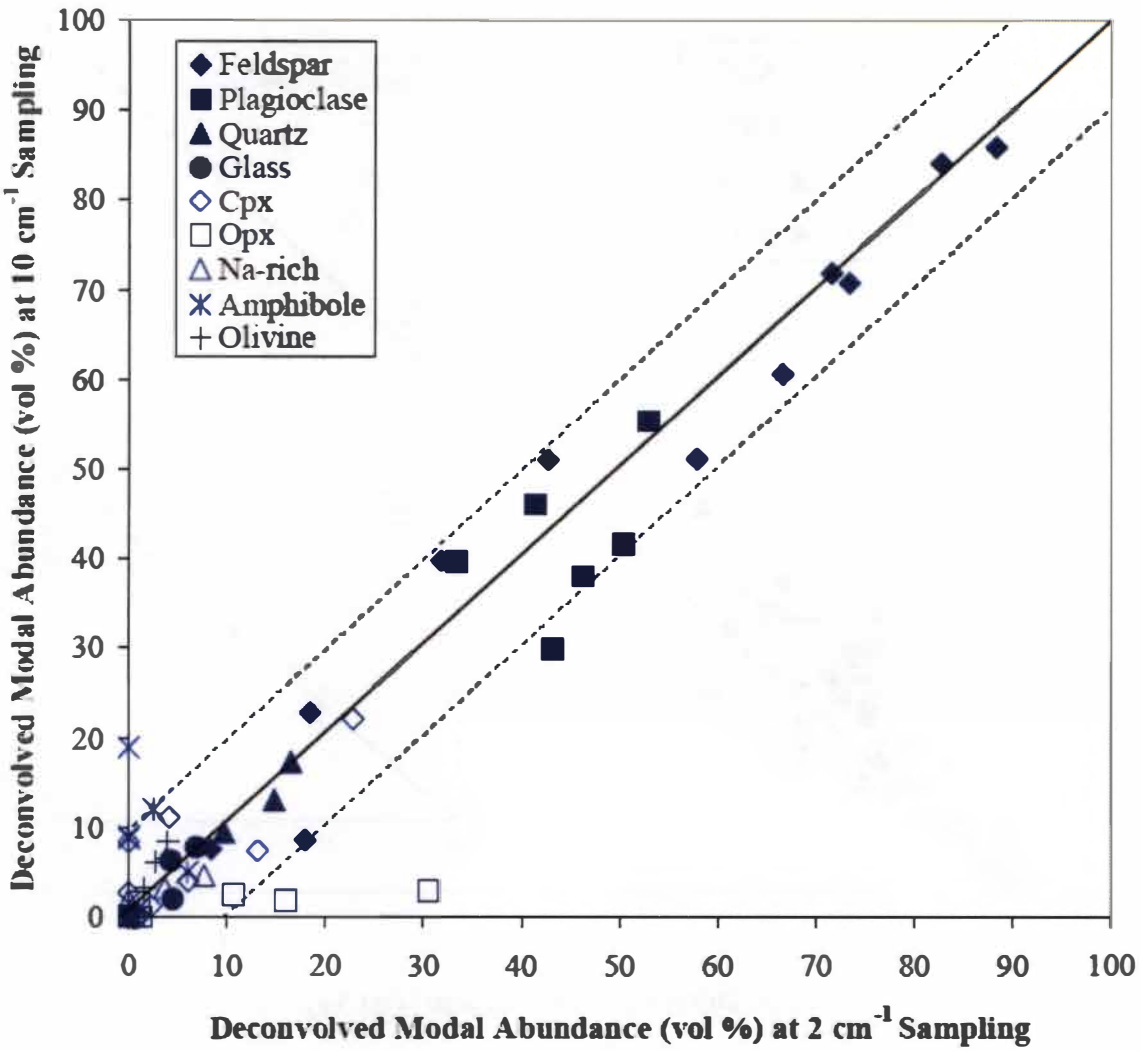


Figure 15. Comparison of modal mineralogy abundances (vol %) at 2 cm^{-1} and 10 cm^{-1} spectral sampling. Dashed lines enclose points that deviate < 10 vol % from the 1:1 line. Uncertainties for each phase are listed in Table 12.

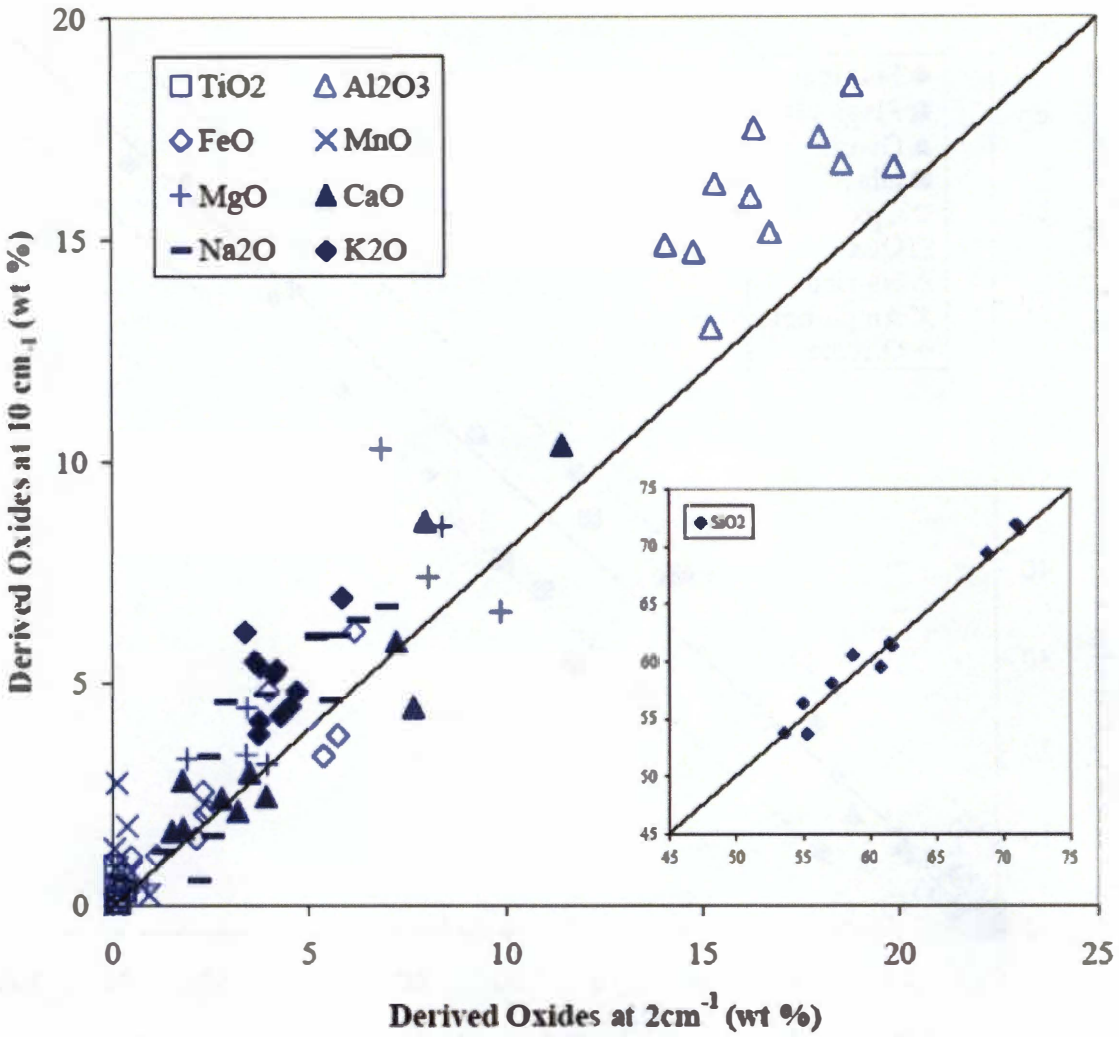


Figure 16. Measured versus derived oxide data (wt %) for basalts, trachyandesites, trachytes, and rhyolites at 2 cm^{-1} and 10 cm^{-1} spectral sampling. Uncertainties for each phase are listed in Table 12.

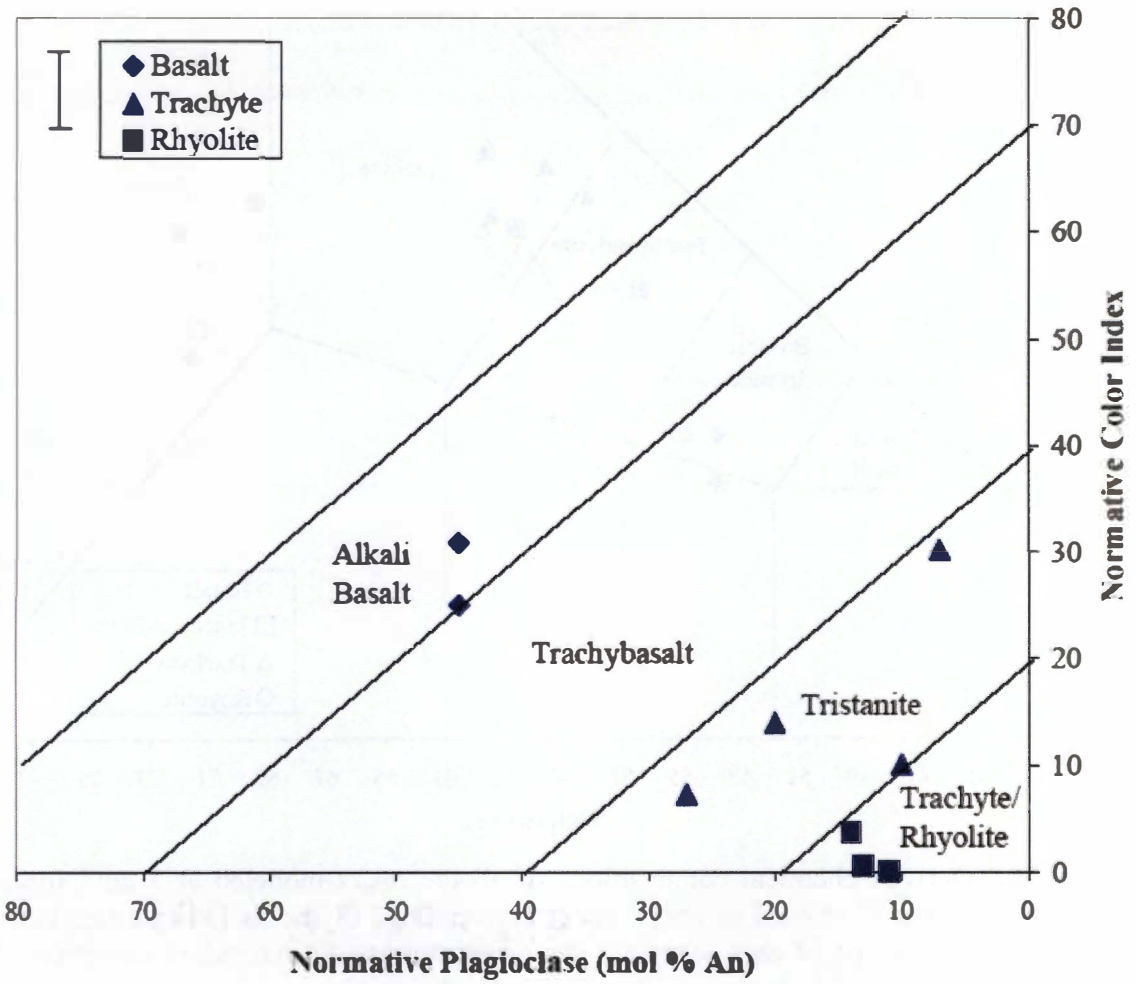


Figure 17. Normative plagioclase compositions (mol % An) versus normative color index (modal olivine + pyroxene + amphibole) [*Irvine and Baragar,* 1971] for data at 10 cm^{-1} spectral sampling. Open symbols indicate measured rock compositions. Error bars for normative color index is the 1σ standard deviation for model-derived phases listed in Table 12.

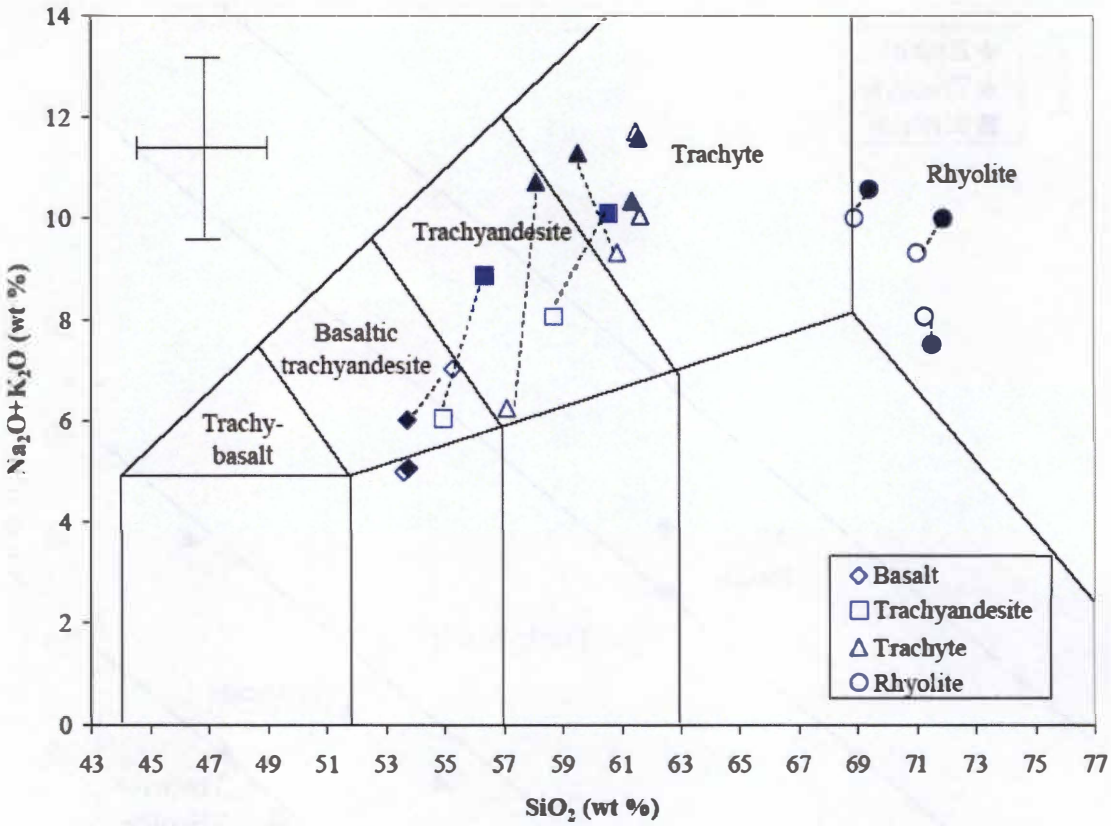


Figure 18. Derived chemical compositions of alkalic rocks modeled at 2 cm^{-1} (open symbols) and 10 cm^{-1} (closed symbols) spectral sampling. Symbols indicate measured chemical classifications of each sample. Error bars represent 1σ standard deviation of silica and alkali oxide abundances at 10 cm^{-1} listed in Table 12.

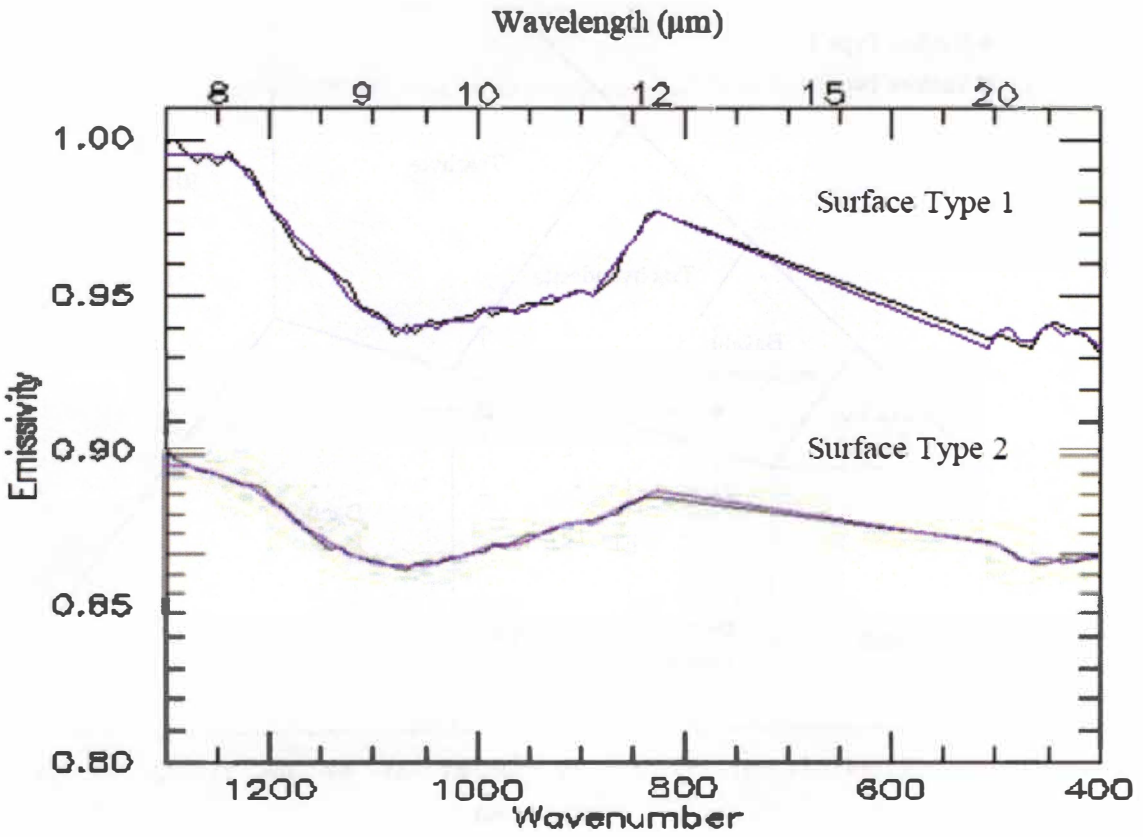


Figure 19. TES martian surface spectra (black) [*Bandfield et al.*, 2000a] and modeled spectra (purple) derived using our alkalic rock end-member set. Spectra are offset 0.1 for clarity.

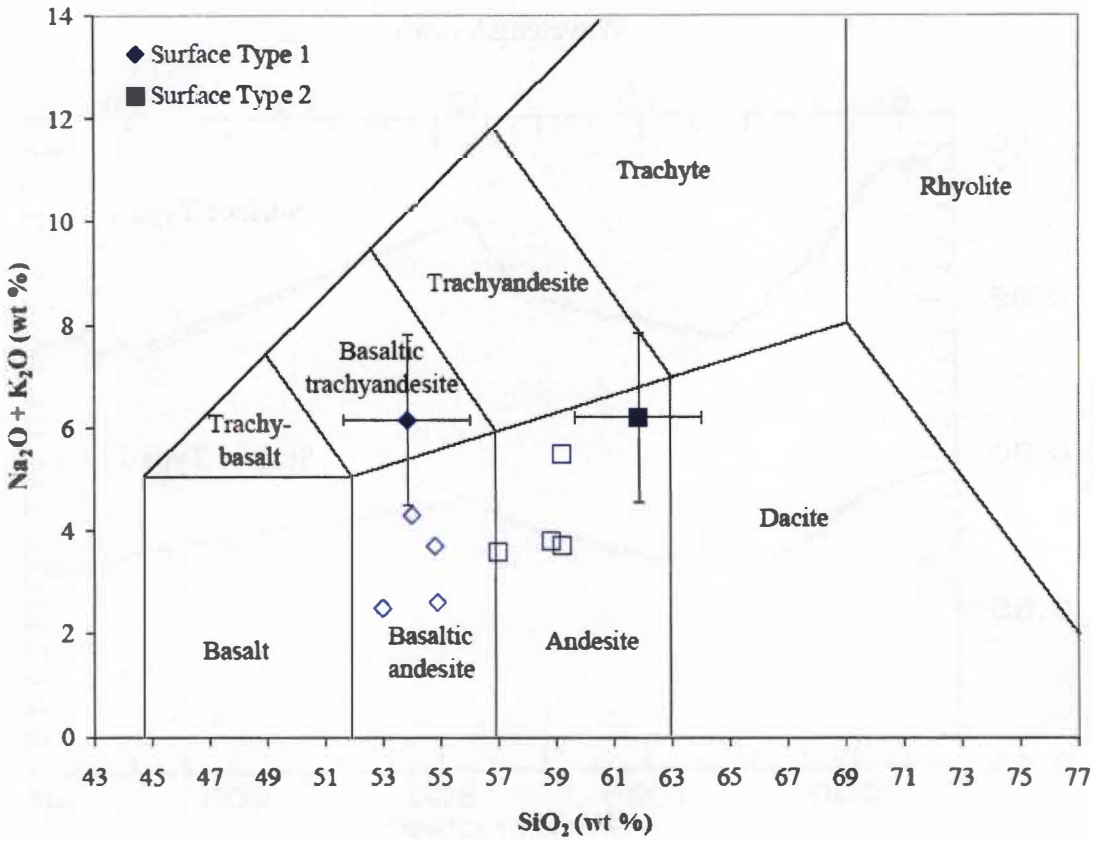


Figure 20. Chemical classification of martian surface type 1 and 2 spectra derived using alkalic end-members. Error bars represent 1σ standard deviation of silica and alkali oxide abundances at 10 cm^{-1} listed in Table 12. Open symbols represent compositions as determined in previous studies [Christensen et al., 2000; Bandfield et al, 2000a].

VITA

Tasha Dunn was born in Atlanta, Georgia on February 25th, 1978. She grew up in the city of Forest Park, a few miles south of Atlanta. As a young child, Tasha developed a strong interest in space exploration and decided to focus her studies in math and science, with hopes of one day becoming an astronaut. Tasha graduated 5th in her class from Forest Park High School in 1996. After high school, Tasha left Georgia to attend Tulane University in New Orleans, Louisiana. In May of 2000, Tasha graduated from Tulane with a Bachelor's of Science degree in Geology, becoming the first college graduate in her family. After college, Tasha moved back to Georgia and worked as a staff geologist and project manager at Consultech Environmental, Inc for three years. In the fall of 2003, Tasha's interest in planetary science brought her back to the academic world, and she entered graduate school at the University of Tennessee to obtain a master's degree in planetary geology. Tasha now resides in Knoxville, Tennessee with her cat, Hugo, and is currently pursuing her Ph.D. at the University of Tennessee.

7695 2036 61
03/08/06 MAR